JGR Atmospheres

RESEARCH ARTICLE
10.1029/2019JD030298

Key Points:
- Polar mesospheric clouds reveal small-scale gravity wave and diverse instability dynamics evolutions at very high resolution
- Gravity waves are always present, but instability forms and intensities depend on gravity waves arising from lower atmosphere weather
- Gravity wave dissipation at PMC altitudes occurs primarily via wave breaking and Kelvin-Helmholtz shear instabilities

Supporting Information:
- Supporting Information S1

Correspondence to:
D. C. Fritts,
dave@gats-inc.com

Citation:
Fritts, D. C., Miller, A. D., Kjellstrand, C. B., Geach, C., Williams, B. P., Kaifler, B., et al. (2019). PMC Turbo: Studying gravity wave and instability dynamics in the summer mesosphere using polar mesospheric cloud imaging and profiling from a stratospheric balloon. *Journal of Geophysical Research: Atmospheres*, *124*, 6423–6443. https://doi.org/10.1029/2019JD030298

Received 11 JAN 2019
Accepted 2 MAY 2019
Accepted article online 17 MAY 2019
Published online 26 JUN 2019

Author Contributions:
Conceptualization: David C. Fritts, Amber D. Miller
Formal analysis: David C. Fritts, Natalie Kaifler, Ling Wang, Sonja Gisinger
Funding acquisition: David C. Fritts
Investigation: C. Bjorn Kjellstrand, Christopher Geach, Bifford P. Williams, Bernd Kaifler, Natalie Kaifler, Glenn Jones, Yucheng Zhao, Gunter Stober, Cora E. Randall
(continued)

PMC Turbo: Studying Gravity Wave and Instability Dynamics in the Summer Mesosphere Using Polar Mesospheric Cloud Imaging and Profiling From a Stratospheric Balloon

David C. Fritts[1], Amber D. Miller[2,3], C. Bjorn Kjellstrand[2], Christopher Geach[4], Bifford P. Williams[1], Bernd Kaifler[5], Natalie Kaifler[5], Glenn Jones[2,6], Markus Rapp[5], Michele Limon[2,7], Jason Reimuller[8], Ling Wang[1], Shaul Hanany[4], Sonja Gisinger[5], Yucheng Zhao[9], Gunter Stober[10], and Cora E. Randall[11]

[1]Boulder Division, GATS, Boulder, CO, USA, [2]Department of Physics, Columbia University, New York, NY, USA, [3]Department of Physics and Astronomy, University of Southern California, Sacramento, CA, USA, [4]School of Physics and Astronomy, University of Minnesota, Minneapolis, MN, USA, [5]German Aerospace Center (DLR), Munich, Germany, [6]Rigetti Computing, Berkeley, CA, USA, [7]Department of Physics and Astronomy, University of Pennsylvania, Philadelphia, PA, USA, [8]Integrated Spaceflight Services, Boulder, CO, USA, [9]Center for Atmospheric and Space Sciences, Utah State University, Logan, UT, USA, [10]Institute of Atmospheric Physics, Kühlungsborn, Germany, [11]Department of Atmospheric and Oceanic Sciences, University of Colorado Boulder, Boulder, CO, USA

Abstract The Polar Mesospheric Cloud Turbulence (PMC Turbo) experiment was designed to observe and quantify the dynamics of small-scale gravity waves (GWs) and instabilities leading to turbulence in the upper mesosphere during polar summer using instruments aboard a stratospheric balloon. The PMC Turbo scientific payload comprised seven high-resolution cameras and a Rayleigh lidar. Overlapping wide and narrow camera field of views from the balloon altitude of ~38 km enabled resolution of features extending from ~20 m to ~100 km at the PMC layer altitude of ~82 km. The Rayleigh lidar provided profiles of temperature below the PMC altitudes and of the PMCs throughout the flight. PMCs were imaged during an ~5.9-day flight from Esrange, Sweden, to Northern Canada in July 2018. These data reveal sensitivity of the PMCs and the dynamics driving their structure and variability to tropospheric weather and larger-scale GWs and tides at the PMC altitudes. Initial results reveal strong modulation of PMC presence and brightness by larger-scale waves, significant variability in the occurrence of GWs and instability dynamics on time scales of hours, and a diversity of small-scale dynamics leading to instabilities and turbulence at smaller scales. At multiple times, the overall field of view was dominated by extensive and nearly continuous GWs and instabilities at horizontal scales from ~2 to 100 km, suggesting sustained turbulence generation and persistence. At other times, GWs were less pronounced and instabilities were localized and/or weaker, but not absent. An overview of the PMC Turbo experiment motivations, scientific goals, and initial results is presented here.

1. Introduction

Gravity waves (GWs), instabilities that arise at large amplitudes, and turbulence that results play central roles in atmospheric dynamics and structure from the surface to over 100 km. The importance of these dynamics is due to the major contributions by GWs to vertical and horizontal transports of momentum from sources at lower altitudes to higher altitudes where momentum deposition accompanies GW dissipation (Bretherton, 1969; Fritts & Alexander, 2003; Holton, 1983; Lilly, 1978; Lilly & Kennedy, 1973; Lindzen, 1981; and references therein). Momentum deposition requires GW dissipation, and below the turbopause at ~105–110 km this requires instabilities and turbulent energy dissipation, ε, apart from weak radiative damping.

Observations and modeling of instability dynamics leading to turbulence have provided valuable insights into GW, instability, and turbulence energetics, transports, and impacts throughout the atmosphere over many years. In the mesosphere and lower thermosphere (MLT), which is our focus here, the major contributions were made by airglow and polar mesospheric cloud (PMC, or noctilucent cloud, if ground based) imaging over a wide range of latitudes (Baumgarten & Fritts, 2014; Dalin et al., 2010, 2019; Fritts, Baumgarten, et al., 2014; Fritts et al., 2017; Miller et al., 2015; Swenson & Mende, 1994; Witt, 1962;

Methodology: David C. Fritts, C. Bjorn Kjellstrand, Christopher Geach, Bifford P. Williams, Bernd Kaifler, Glenn Jones, Michele Limon, Jason Reimuller, Ling Wang, Shaul Hanany, Gunter Stober
Resources: Amber D. Miller, Markus Rapp, Shaul Hanany
Supervision: David C. Fritts, Amber D. Miller, Markus Rapp
Visualization: Ling Wang, Sonja Gisinger
Writing - original draft: David C. Fritts

Yamada et al., 2001). More recent contributions by radar and lidar profiling (Franke & Collins, 2003; Lehmacher et al., 2007; Pfrommer et al., 2009) and especially in combination with ground-based or airborne imaging (Eckermann et al., 2016; Fritts, Vosper, et al., 2018; Hecht et al., 1997, 2018, 2005, 2014; Pautet et al., 2016) have revealed instability character, spatial and temporal scales, and evidence of the environments in which they arose.

Instabilities arising due to GWs take various forms, depending on the GW character, amplitude, and environment (Lombard & Riley, 1996; Sonmor & Klaassen, 1997; Staquet & Sommeria, 2002). Observations have provided evidence of overturning and breaking of GWs having relatively high intrinsic frequencies at altitudes from the troposphere into the MLT (Eckermann et al., 2016; Franke & Collins, 2003; Fritts et al., 1993, 2017; Fritts, Vosper, et al., 2018; Hecht et al., 1997; Lilly & Kennedy, 1973; Swenson & Mende, 1994; Triplett et al., 2018; Whiteway et al., 2003; Witt, 1962). In contrast, GWs having near-inertial frequencies are expected and observed to exhibit Kelvin-Helmholtz instabilities (KHI; Lelong & Dunkerton, 1998a, 1998b; Pavelin et al., 2001; Stober et al., 2018). These same dynamics arise in oceans and lakes (Thorpe, 1977; Woods, 1968; Woods & Wiley, 1972) and have been studied in the laboratory (Thorpe, 1973a; also see the reviews by Thorpe, 1973b, 2005). Additionally, GWs having significant amplitudes and momentum fluxes can exhibit strong interactions with the local mean flow. These manifest as "self-acceleration" events that have been modeled under idealized and more realistic conditions (Dosser & Sutherland, 2011; Fritts et al., 2015; Fritts, Laughman, et al., 2018; Fritts, Wang, et al., 2018; Sutherland, 2001, 2006) and that have recently been identified in the MLT OH airglow layer and by the Polar Mesospheric Cloud Turbulence (PMC Turbo) experiment, to be reported separately.

Superpositions of lower- and higher-frequency motions, which we will refer to as multiscale dynamics (MSD), are ubiquitous throughout the atmosphere and yield these same dynamics, but as responses that are spatially localized. Examples include local GW breaking (Hecht et al., 2018; Yamada et al., 2001) and local, and often strongly modulated, KHI (Baumgarten & Fritts, 2014; Eaton et al., 1995; Fritts & Rastogi, 1985; Fritts, Baumgarten, et al., 2014; Fritts, Wan, et al., 2014; Fritts et al., 2017; Hecht et al., 2005, 2014, 2018; Lehmacher et al., 2007; Pfrommer et al., 2009; Thorpe, 1987, 2002; Witt, 1962). Recent, high-resolution MSD modeling has exhibited localized GW breaking, revealed a mechanism for strong, local KHI on enhanced shears induced by GW breaking events, captured other events leading to turbulence that were identified as intrusions, and demonstrated GW trapping and instability dynamics in an inversion layer (Fritts et al., 2013, 2016; Fritts, Laughman, et al., 2018; Fritts, Wang, et al., 2018). Clear examples of idealized GW breaking and several MSD instability events were observed recently in serendipitous high-resolution imaging of PMCs by star cameras on the EBEX cosmology experiment flown on a long-duration balloon (Fritts et al., 2017; Miller et al., 2015).

In many cases, specific instability dynamics appear to allow reasonably quantitative assessments of instability evolutions, time scales, and energetics. In cases of GW breaking, direct numerical simulations (DNS) of idealized flows have revealed specific pathways from large-amplitude, monochromatic GWs through transitional instabilities to turbulence. These have demonstrated initial streamwise-aligned (along the propagation direction), counterrotating vortices that intensify, link to adjacent vortices, and evolve to initial "horse-shoe" vortices and successive vortex rings (Andreassen et al., 1998; Fritts et al., 1998, 1994). More recent DNS addressing higher Reynolds numbers that are more representative of instabilities extending from low altitudes into the mesosphere have revealed the further rapid evolution of vortex rings via mutual vortex interactions to nearly isotropic turbulence at smaller spatial scales (Fritts et al., 2009a, 2009b). Comparisons of these GW breaking dynamics predictions with specific observations of PMCs and OH airglow layers have yielded close agreement in the form, evolution, and time scales in several cases (Fritts et al., 1993, 2017; Hecht et al., 2018; Miller et al., 2015). Indeed, the first evidence of these features was provided by Witt (1962, Figure 12a) and Yamada et al. (2001, Figure 1, beginning ~17:01 UT), though these features were not identified as vortex rings by those authors. Importantly, however, Witt (1962) successfully identified the dominant GW and KHI features in his stereo ground-based PMC observations ~60 years ago.

Applications of DNS to KHI for various Reynolds and Richardson numbers, *Re* and *Ri*, respectively, for idealized shear flows and MSD arising from superposed higher- and lower-frequency motions have yielded other comparisons that provide further evidence of the validity of DNS descriptions of such

flows. Specifically, comparisons of PMC and OH airglow imaging and modeling have revealed tendencies for enhanced KHI accompanying significant GW amplitudes (Baumgarten & Fritts, 2014; Fritts, Baumgarten, et al., 2014; Fritts, Wan, et al., 2014; Hecht et al., 2014, 2018). These features are consistent with regions of preferred KHI capping local GW breaking in MSD (Fritts et al., 2013) and apparent in radar and lidar profiling noted above. PMC and airglow imaging have also revealed features aligned along the plane of Kelvin-Helmholtz (KH) billow rotation that intensify, interact, and ultimately break down to smaller-scale turbulence (Baumgarten & Fritts, 2014; Hecht et al., 2014). These secondary instability features comprise counterrotating vortices, with spanwise (normal to the evolution plane) wave numbers, that arise in the outer (inner) portions of the KH billows for smaller (larger) *Ri* that are relatively more (less) unstable (Fritts, Baumgarten, et al., 2014; Fritts, Wan, et al., 2014). Of these, the events exhibiting the most rapid evolutions are those having the smallest *Ri*, the deepest KH billows, and the largest *Re*.

Finally, PMC imaging has revealed features subsequently found in the MSD modeling and others first identified in MSD modeling and subsequently found in EBEX or ground-based PMC imaging. One category includes what we referred to above as intrusions and comprise fronts that are initially laminar but ultimately become turbulent. A second category includes events that appear to contain multiple cusp-like features that arise at the lower edge of GW breaking in an MSD environment. There are also many interesting EBEX PMC images exhibiting smooth, apparently laminar features and others having strong, complex or turbulent features for which the underlying dynamics were not identified due to the lack of temporal imaging of these events.

Importantly, transitional instabilities that have been quantified in PMC and OH airglow imaging have enabled quantitative estimates of the underlying dynamics in the various DNS, including specific GW, KHI, and/or MSD character and scales. These enabled, in turn, quantitative estimates of ε and more qualitative estimates of the turbulent kinematic viscosity based on the corresponding DNS instability scales and turbulence intensities (Fritts et al., 2017; Fritts, Baumgarten, et al., 2014; Hecht et al., 2014, 2018). In particular, ε inferred from EBEX and ground-based PMC imaging by Fritts et al. (2017) for various idealized and MSD events were in the range of those estimated in multiple in situ rocket measurement programs and occasionally very large.

The limited comparisons of PMC imaging and modeling to date have suggested a potential to dramatically enhance our understanding of the morphologies of small-scale dynamics leading to turbulence by imaging PMCs continuously at high resolution from the stratosphere. Specifically, the ability to image the dynamics leading to turbulence at scales extending from GW energy inputs at horizontal wavelengths of $\lambda_h \sim$ 20–100 km, through various instabilities, to an inner scale of turbulence as small as $l_0 \sim$ 10–20 m appears to be unique to the PMC layer (see Fritts et al., 2017; Miller et al., 2015). There are limitations to ground-based PMC and airglow imaging, however. Both are confined to nighttime or twilight conditions and cloud-free viewing and hence cannot observe full diurnal cycles. Ground-based PMC viewing is typically best for low elevation angles, ~30° or lower and thus has the potential to cause ambiguous interpretations of feature scales and orientations in the horizontal and vertical (see Baumgarten & Fritts, 2014). Lastly, it is usually not supported by vertical profiling of local winds, temperatures, or PMCs.

Our motivations for the PMC Turbo experiment included the following:

1. exploration of MLT GW and instability dynamics continuously for multiple days spanning variable tropospheric weather and GW filtering by stratospheric winds and
2. acquisition of expanded and diverse PMC imaging enabling additional comparisons with modeling and further quantification of the multiple pathways to geophysical turbulence.

Our PMC Turbo overview is organized as follows. The design, capabilities, and demonstration of the PMC Turbo imaging and profiling systems are described in section 2. Evolutions of tropospheric weather, stratospheric and mesospheric winds, mesospheric temperatures, the northern polar PMC field throughout the PMC Turbo flight, and their implications for PMC Turbo observations are presented in section 3. Sections 4 and 5 describe the global context of our measurements and provide examples of PMC Turbo dynamics events highlighting the diversity of the responses. A discussion of these results in the context of previous studies is provided in section 6. Our summary and conclusions are presented in section 7.

Figure 1. The PMC Turbo payload ready to launch (B. Kaifler photo).

2. PMC Turbo Payload and Imaging and Profiling Capabilities

2.1. Payload

The PMC Turbo payload (Figure 1) included the scientific instruments, solar panels and power system, the National Aeronautics and Space Administration (NASA) control and communication systems, a rotator maintaining anti-Sun viewing, and 450 kg of ballast to drop, as needed, in order to maintain a mean altitude of ~38 km. Science instruments included seven imaging systems and a Rayleigh lidar. Each imaging system was in a pressure vessel that included an ~16-megapixel camera, a 50- or 135-mm lens yielding a wide or narrow field of view (FOV), a control computer, and four 8-TB hard drives for data storage. The lidar transmitter, electronics, control, and data storage systems were in a larger pressure vessel, and the 0.5-m lidar telescope was mounted separately. These instruments yielded ~125 TB of data (including ~6,000,000 camera images, of which >2,000,000 showed PMCs) over the ~5.9-day PMC Turbo flight from launch at 7:28 UT on 8 July at Esrange in Sweden (67.9°N, 21.1°E) to landing at 5:37 UT on 14 July in Northern Canada (66.8°N, 109.4°W). The payload and instruments will be described in other papers currently in preparation. A list of the payload components and their specifications is provided in Table 1.

2.2. Imaging and Profiling Capabilities

2.2.1. PMC Imaging

Four wide-FOV cameras on the PMC Turbo gondola were configured to span a composite FOV of ~80 × 120 km at the ~82-km PMC altitude. Three narrow-FOV cameras were positioned to image the regions of overlap of the wide-FOV imaging nearest zenith viewing at higher resolution. Individual FOVs for the seven cameras are shown in Figure 2. Decreasing resolution is only significant for the wider FOVs because they image to much larger off-zenith angles. With this viewing geometry, the wide-FOV resolution varied from ~10 m near zenith to ~20 m at the lowest elevation angles, whereas the narrow-FOV resolution was ~4 m, though motion blur (see below) most often degraded the effective resolution. The mean imaging cadence was ~2 Hz for all cameras, including a two- to four-image burst mode intended to allow coadding of sequential images after motion correction to improve image signal to noise.

Motion blur was caused by several factors. The gondola had the potential for both rotation and pendulation. However, a NASA rotator between the gondola and the balloon constrained gondola rotation to a very high degree; hence, rotation had an insignificant influence. Pendulation of period ~20 s yielded larger angular imaging variations, with apparent induced motions as large as 50 m/s, hence a blur of ~5–30 m for ~100- to 600-ms exposures. Mean motions of the PMC layer were nearly aligned with the gondola drift velocity, but variable mean, tidal, and GW motions induced apparent PMC motions of ~50 m/s, hence comparable to those due to pendulation. Better resolution occurred randomly where the various sources of motion blur were small or tended to cancel. Hence, true resolution was best during the brightest events.

Two examples of the composite FOV images are shown in Figure 3. The composite images span the horizontal GW scales most likely to induce instabilities at smaller scales. The image in Figure 3a shows multiple examples of the instability dynamics leading to vortex rings at various scales, which are indicative of GW breaking accompanying different GW events and scales in different regions (see Fritts et al., 2017, for further discussion of these dynamics). The image in Figure 3b exhibits KHI having ~4-km wavelengths (see upper left half of Figure 3b), very small scale secondary convective instabilities within, and secondary KHI along the outer edges of, the ~4-km KH billows, and additional instabilities accompanying KH billow interactions (as discussed by Thorpe, 2002) where they are misaligned along their axes, especially in the upper left region in Figure 3b. Larger-scale GW dynamics, which are important in these fields, are suppressed in these images by flat fielding (see below), enabling higher sensitivity to the smaller spatial scales. Such imaging was

Table 1
PMC Turbo Experiment Payload Components

Component	Specifications/comments
Cameras (7)	Allied Vision Prosilica GT 4907, Kodak 16070 CCD (3,232 × 4,864 pixels), shutterless, high frame rate, burst-mode options, custom auto-exposure algorithm.
Camera lenses	Canon 50 mm f1.2 (4), Canon 135 mm f/2 (3), L series, apochromatic.
Camera computers (7)	Supermicro ITX Server boards with Intel atom processor, 3X redundant RAID OS on SSD and spinning disk partitions, attached labjacks monitor housekeeping.
Data storage	Twenty-eight 8-Tb Seagate drives, 32 TB for each imaging system.
Pressure vessels	0.5″ Al cylinders (7), powder coated, 1,200-hPa pressure, each hosting a camera, lens, computer, 32-TB storage, full system software control/comms./data link.
Camera software	Linux OS, camera interface written in C, image processing, telemetry, and flight control written in Python, distributed flight control capability for redundancy.
Camera network	Resilient coordinated network of computers, Gigabit Ethernet, synchronized image capture to ~10 ms, serial-to-ethernet interface with NASA SIP.
Rayleigh lidar transmitter and receiver	532-nm wavelength, 100-Hz PRF, 45 mJ/pulse, 5-ns pulse length, fiber coupled, 0.3-nm bandwidth, photon-counting avalanche photo diodes, active thermal control, 1.6-m^2 radiator, commercial flight computer with i5 processor, 1-TB redundant flash storage, FPGA-based I/O controller, Linux OS, C++ software.
Telescope	0.5-m f/2.4 quartz mirror, protected Al coating, 165-μrad FOV.
Power system	Suncat solar panels (15), TriStar MPPT 60 A charge controllers, Valence U1-24RT batteries, 1,370-W in two circuits, split camera and lidar loads, redundancy against a single circuit failure, switchable loads, 2-kWh battery ascent backup. Relay boards connected directly to NASA SIP provide analog housekeeping over power umbilicals and direct power control.
NASA SIP	Support Instrumentation Package, separate power system, TDRSS and Iridium comms. for flight control and data links at ~100 kbps, multiple redundant channels.

possible where PMCs were sufficiently bright and occurred ~50% of the time along the flight track from Esrange, Sweden, to Northern Canada (see Figure 4).

Flat fielding included the following elements for each imaging system:

1. preflight definition of a dark image (D) to account for dark current across the array;
2. preflight definition of a mean flat field (F) from twilight images with varying brightness;
3. simulation of sky brightness (S) at float altitude;
4. initial flat-field estimate for initial image I defined as $I' = (I - D)\,(\text{mean } F)/F - S$ to compensate for vignetting and remove sky brightness;
5. division by exposure time to calibrate response, as exposure time varied temporally and between cameras; and
6. subtraction of a moving average image to compensate for scattered light.

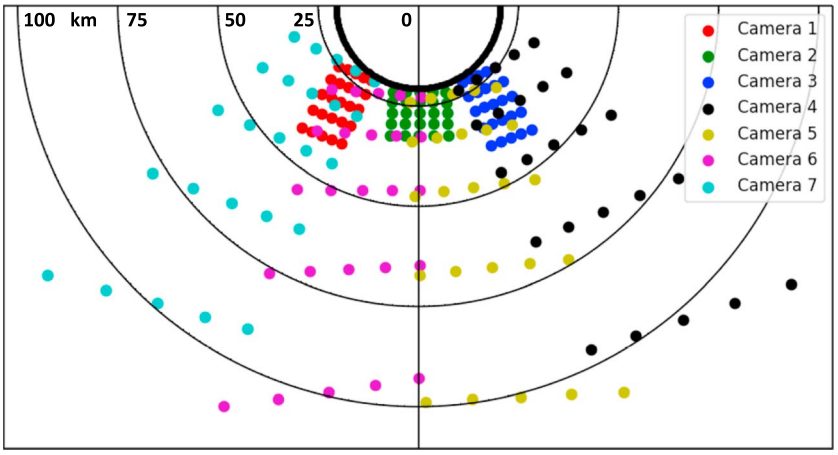

Figure 2. Fields of view of the seven PMC Turbo cameras viewed from above (legend in inset). Dots indicate uniform spacing in the camera images and the decreasing resolution at larger off-zenith angles.

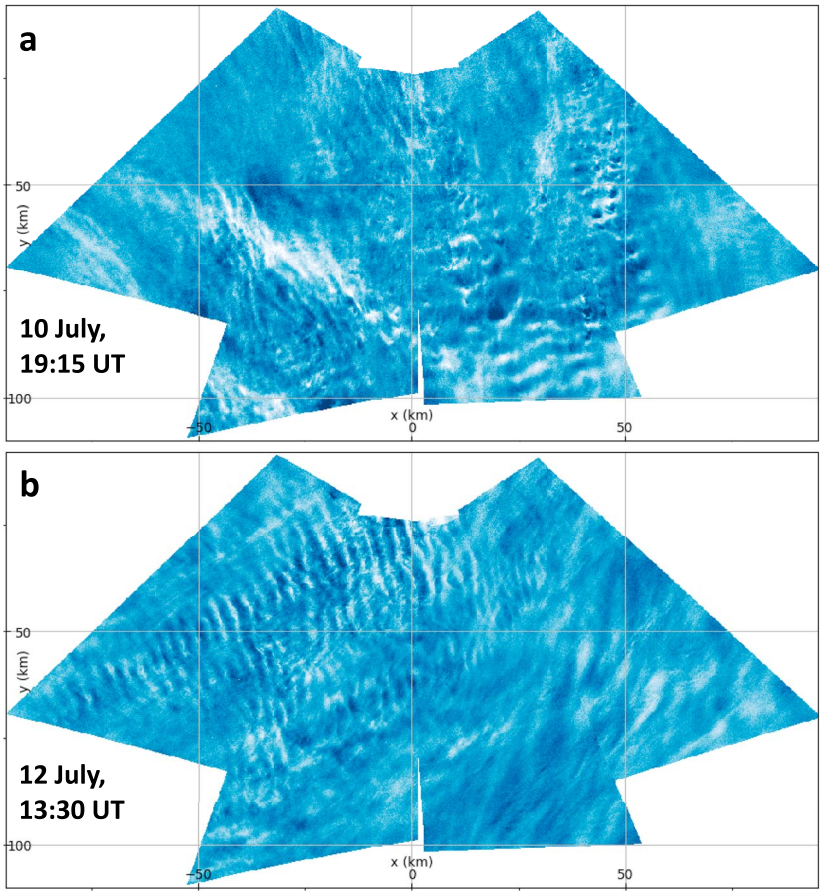

Figure 3. Composite wide-FOV images showing (a) extensive GW breaking at multiple scales at 19:15 UT on 10 July and (b) KHI evolution and breakdown at 13:35 UT on 12 July 2018 viewed from below. Each image reveals significant variability suggesting spatial modulation of the instability dynamics by larger-scale GWs.

2.2.2. PMC Lidar Profiling

A solid-state Rayleigh lidar was contributed to the PMC Turbo payload by the German Aerospace Center. The Balloon Lidar Experiment (BOLIDE) was the first high-power lidar to operate from a stratospheric balloon. It pointed 28° off zenith within the FOVs of cameras 2 and 5 (see Figure 2). It transmitted 4.5 W at 532

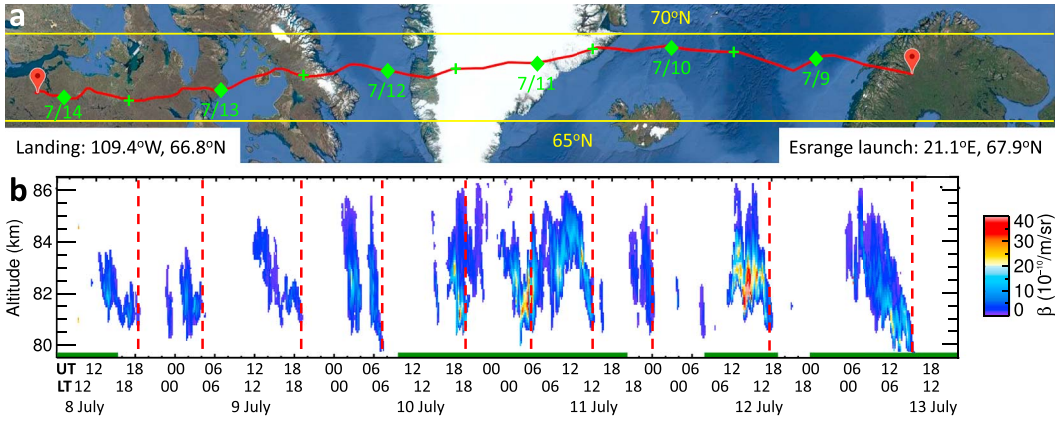

Figure 4. (a) PMC Turbo flight track from Esrange to Northern Canada (diamonds are at 00 UT). (b) Rayleigh lidar PMC detections throughout the PMC Turbo flight. Dashed red lines show disappearance of the PMC events. Green lines at the bottom show times over land (map: Google).

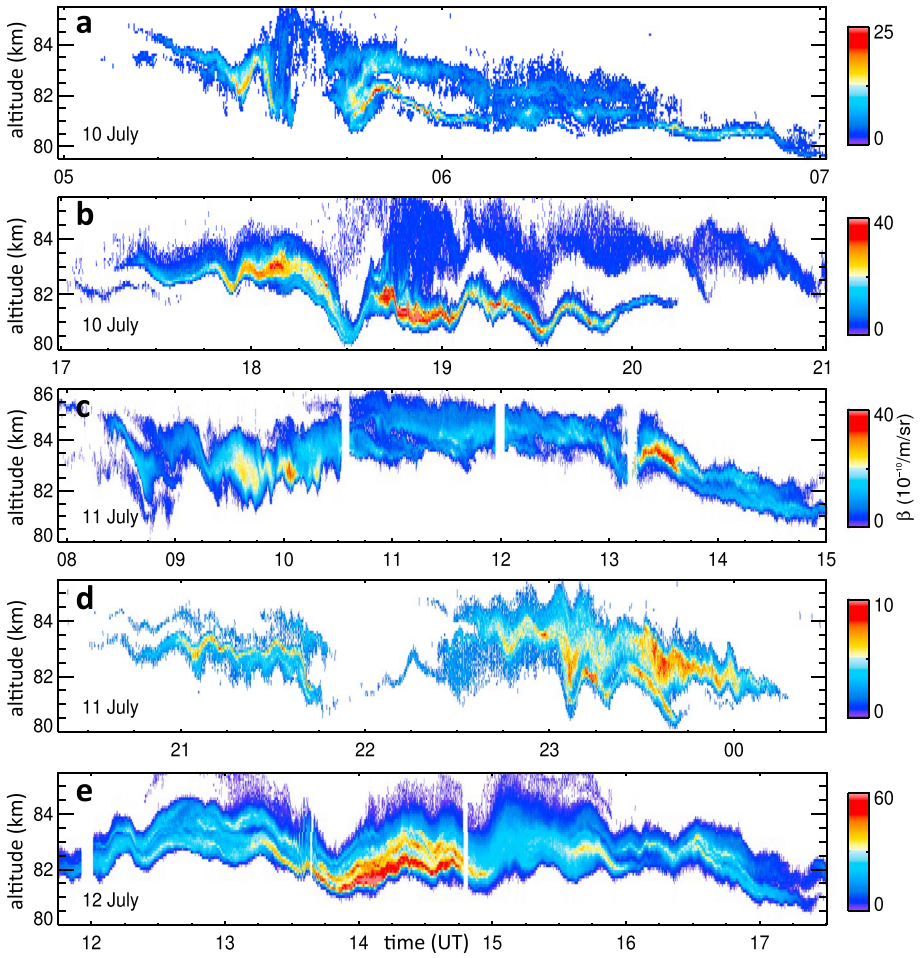

Figure 5. (a–e) Lidar PMC backscatter in five intervals exhibiting significant modulations in altitude. Backscatter was obtained from averages over 100 m in altitude and 10 s.

nm, had a pulse repetition frequency of 100 Hz, had a pulse length of 1.5 m (5 ns), and employed a 0.5-m-diameter mirror for received photons. Cross sections of PMC backscatter and vertical displacements for five intervals are shown in Figure 5.

The Rayleigh lidar also measured the temperature profile, $T(z)$, and perturbations, $T'(z)$, from ~52–80 km throughout the flight using hydrostatic integration of the backscatter profiles (Kaifler et al., 2015) with an initial mean T from the Microwave Limb Sounder aboard the Aura satellite below the PMC layer. The mean lidar $T(z)$ was found to agree with the mean Microwave Limb Sounder $T(z)$ to within 5 K where confident estimates were obtained at lower altitudes. It is not shown because $T(z)$ estimates were not confident sufficiently close to the PMC layer. Lidar $T'(z, t)$ cross sections for the full flight and for 12 July are shown in Figure 6.

Lidar PMC observations in Figure 5 reveal the PMC layer to have been highly variable, with multiple instances of two or more layers, sometimes very thin, other times deep and diffuse. Distinct layers persisting for hours and having uniform spacing despite shorter-period altitude excursions suggest possible temperature minima (maxima) at successive cold (warm) phases of lower-frequency GWs having vertical wavelengths of λ_z ~ 1–2 km. While having small $T' \sim -(dT/dz + g/c_p)\delta z$ for vertical displacement δz (assuming GW saturation constrains GW amplitudes), a sustained T' variation in altitude can nevertheless impact PMC particle growth or sublimation and hence influence PMC brightness profiles over multiple hours, especially at the lower altitudes where they are highly susceptible to mean T variations.

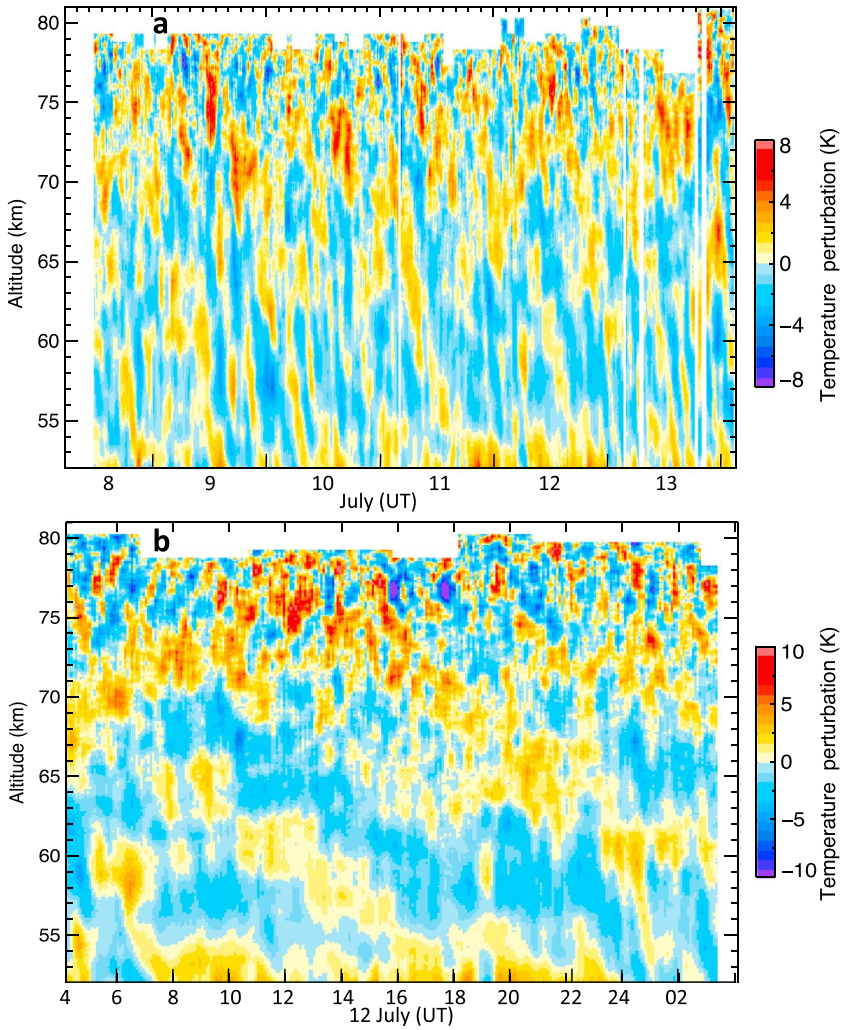

Figure 6. Rayleigh lidar $T'(z, t)$ exhibiting GW responses for the (a) full flight duration and (b) 23 hr on 12–13 July. $T'(z)$ were derived using a Butterworth filter with a 15-km cutoff, 1.3-km averaging in z, and 60-min (20-min) averaging for the full (partial) data set.

Motions at shorter periods of ~10–60 min imply higher-frequency GWs with vertical wavelengths λ_z ~ 5–10 km or somewhat larger. This is because GW breaking instabilities typically limit vertical displacements to $\zeta' = w'/\omega_i \sim \lambda_z/2\pi$ for hydrostatic GWs, where w' and ω_i are the GW vertical velocity and intrinsic frequency, respectively, $\omega_i = kc_i = k(c - U)$, $k = 2\pi/\lambda_h$, and c and U are the ground-based phase speed and mean wind in the plane of GW propagation, respectively (Fritts et al., 2017). A caveat is that high-frequency GW ω_i, c_i, and intrinsic periods, $T_i = 2\pi/\omega_i$, are uncertain given that U and the GW phase orientation are not known. However, GWs having short observed periods must have high intrinsic frequencies because realistic mean winds cannot Doppler shift very small ω_i to large apparent values.

Even shorter periods of ~10 min or less are evidence of small-scale instabilities accompanying GW breaking or KHI advecting with the large-scale flow, such as that seen in the PMC Turbo images in Figure 3, or GW having high ω_i potentially Doppler shifted to even higher observed frequencies, $\omega = kc = \omega_i + kU$, in cases where U is along c, where c and U are relative to the PMC Turbo reference frame.

Turning to the lidar $T'(z, t)$ cross sections in Figure 6, we see that GWs having observed periods of ~4–12 hr dominate from near the stratopause at ~50 km (see Figure 9j below) to ~70 km. The opposite is the case in the upper mesosphere near PMC altitudes, where lidar T' suggest observed GW periods of T_{GW} ~ 1 hr and less. And the transition in dominant GW periods occurs at altitudes between ~65 and 75 km.

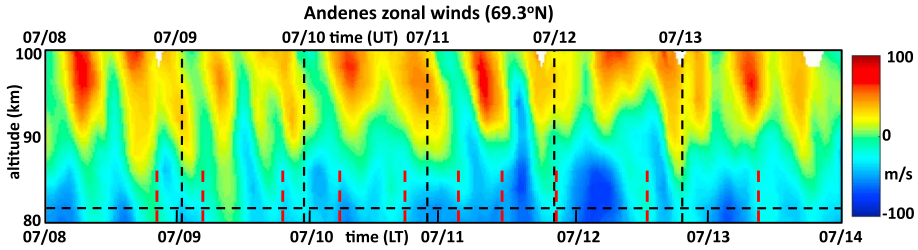

Figure 7. Tidal, planetary wave, and mean winds spanning the PMC Turbo flight. Note the strong SDT amplitudes at earlier times. Dashed red lines show disappearance of the polar mesospheric cloud events in Figure 4.

There is a plausible explanation for the transition in observed GW periods and T' seen in Figure 6. The mean temperature gradient at these altitudes is expected to be about −3 K/km (see Figure 8j), implying a GW T' ~ 6 K for an ~1-km vertical displacement. The observed peak T' and inferred ~1-km displacement suggest GW amplitudes approaching those required for instabilities and dissipation for GW λ_z ~ 6 km or somewhat larger. Figures 6a and 6b reveal that the low-frequency GW λ_z generally decrease from ~10–15 km below 65 km to ~5–10 km above 65 km, suggesting preferential propagation toward decreasing $c_i = (c - U)$, hence generally westward propagation in increasing westward U, and an expectation of GW dissipation below the westward U maximum. One consequence of GW breaking and dissipation is the generation of secondary GWs (SGWs) having smaller λ_h, larger ω_i, and increasing T' with increasing altitude (Bossert et al., 2017; Heale et al., 2017), all of which are consistent with the T' fields shown in Figure 6. The presence of this behavior throughout the PMC Turbo flight suggests that SGWs may be a primary driver of the various instability dynamics seen in the PMC imaging at ~81–84 km.

There is also some evidence in the T' fields for large-scale GW phases ascending in time. These cannot be GWs propagating downward over large depths, as they would necessarily experience large amplitude reductions due to increasing density, which is not observed. Instead, they are likely GWs having propagation directions and phase speeds at least somewhat opposed to the mean U at these altitudes. In such cases having westward c but eastward $c_i = (c - U)$, the true downward phase progression in time would be Doppler shifted to an apparent upward phase progression, as observed. Additionally, such GWs would also experience an increasing λ_z with increasing altitude, for which there is some evidence in Figure 6a (see the upward and rightward phases at ~60–75 km from 10 to 12 July).

2.2.3. PMC Event Variability

Here we examine the factors that appear to influence PMC occurrence and GW and instability activity seen in the PMC imaging on longer time scales. PMC occurrence shown in Figure 4b exhibits strong intraday and interday variability, with the dominant modulation having a semidiurnal response from launch through 11 July and a more nearly diurnal modulation thereafter. The majority of these PMC events disappear accompanying their descent to ~80–82 km. This late-stage behavior is also seen in all of the events shown in Figure 5. These features are consistent with expected strong semidiurnal tide (SDT) and weaker diurnal tide (DT) responses, which cause cooling (warming) during ascending (descending) phases. The SDT in particular can achieve T' ~ 20 K at these latitudes and altitudes (Williams et al., 2006) and contributes strongly to PMC particle growth (or sublimation) at the PMC layer due to ascending (descending) motions.

Evidence for SDT and DT influences are confirmed by low-pass meteor radar winds retaining the SDT and longer-period motions over ALOMAR (Arctic Lidar Observatory for Middle Atmosphere Research; 69.3°N, Norway), shown in Figure 7, spanning the PMC Turbo flight. These reveal an initial SDT having a zonal wind amplitude as large as u' ~ 15–30 m/s at 82 km and λ_z ~ 100 km estimated from phase variations in altitude. The SDT u' and λ_h ~ 7,070 km at 69.3°N imply SDT vertical velocities as large as $w' \sim u'\lambda_z/\lambda_x$ ~ 0.2–0.4 m/s, vertical displacements as large as ~1.4–2.8 km, and adiabatic cooling or heating by tidal motions exceeding ~10–20 K, apart from radiative effects. Daily-mean zonal winds are westward and vary from ~30 to 50 m/s over the PMC Turbo flight, thus significantly more westward than the PMC Turbo westward drift speed of ~10–12 m/s at ~38 km.

Direct comparisons between radar eastward (and inferred descending) motions and the disappearance of PMC backscatter at ~80–82 km are shown with red dashed lines in Figures 4b and 7. Because MLT winds

were measured over ALOMAR, we assumed a migrating SDT and a common LT phase at ALOMAR and at the balloon location as it drifted west to assess these correlations. Specifically, they suggest a significant SDT influence at earlier times and other large-scale (primarily DT) motions when they occur, which largely dictate the occurrence (and especially the disappearance) of strong PMCs at these latitudes throughout the PMC season. The PMC correlations with the SDT seen earlier in the PMC Turbo flight are consistent with those observed in previous satellite and ground-based lidar studies (Stevens et al., 2017; Fiedler et al., 2011). In each case, the disappearance of PMCs accompanied, or slightly lagged, the largest eastward winds (and implied downward winds and warming) at ~80–82 km.

We now examine the variability in the dynamics revealed in the PMC layer throughout the PMC Turbo flight. The composite wide-FOV images in Figure 3 show examples of extensive GW breaking instabilities and KHI evolution and breakdown, but there are many other types as well. The various dynamics seen in PMC Turbo imaging include the following:

1. diverse GW superpositions with and without apparent smaller-scale instabilities;
2. KHI at larger and smaller scales, sometimes exhibiting instabilities, other times not;
3. instability forms arising from GW breaking and KHI, some observed previously and predicted or reproduced in modeling studies addressing these dynamics;
4. large-scale coherent structures suggestive of mesospheric bores and/or GW fronts;
5. evidence of GW self-acceleration dynamics and SGW generation; and
6. multiple dynamics and structures that remain to be identified and explained.

Dynamics tentatively identified, but requiring more detailed analyses and modeling efforts, for each of the major PMC events seen in Figure 4b are summarized in Table 2. These dynamics exhibit highly variable character, scales, and intensities throughout the PMC Turbo flight, suggesting modulation of the GW and instability dynamics seen by PMC Turbo by GW source and propagation conditions at lower altitudes. Of these dynamics, we expect the strongest MLT forcing to accompany the breaking of GWs having large λ_z ~ 10–20 km, small λ_h ~ 20–100 km, and large ω_i because these GWs have the largest vertical group velocities and account for the largest energy and momentum fluxes into the MLT. In contrast, instabilities accompanying larger-horizontal-scale GWs, such as those trailing GW fronts and bores, or KHI arising at enhanced shears due to lower-frequency GW superpositions, while impressive, do not account for rapid GW dissipation or strong energy and momentum deposition. The various dynamics listed in Table 1 vary strongly over the PMC Turbo flight duration. Dynamics at the PMC layer were seen to be relatively weak until ~15 UT on 9 July, after which they appeared to increase in intensity. They remained strong, implying strong MLT forcing, until after ~15 UT on 11 July, and were much weaker thereafter, except for strong dynamics and instabilities from ~13 to 16 UT on 12 July.

3. Tropospheric Weather, Stratospheric Fields, and Their Implications

3.1. Tropospheric Weather

Weather events in the troposphere and lower stratosphere, such as airflow over orography, convection, fronts, and jet streams, are known to excite GWs that are able to propagate into the stratosphere and to higher altitudes under suitable environmental conditions (Fritts & Alexander, 2003; Plougonven & Zhang, 2014). Of these, polar low-pressure systems, or "polar lows," and their associated jet streams convection, and orographic forcing were likely the major tropospheric sources of GWs during the PMC Turbo flight. The evolution of these large-scale dynamics occurring as PMC Turbo drifted north of Iceland and over Greenland is illustrated in Figure 8. Figures 8a–8h show European Centre for Medium-Range Weather Forecasting (ECMWF) analyses of horizontal winds and geopotential heights at 00 and 12 UT on 10 and 11 July at 700 and 200 hPa. These dynamics include a strong but decreasing jet stream aligned toward the NNE over Iceland and an intensifying polar low crossing Southern Greenland at these times.

Strengthening of the jet stream east of the Greenland coast toward the NE and its extension down to the Iceland terrain prior to ~00 UT on 10 July were likely significant contributors to the strong increases in GWs and instabilities seen in the PMC layer beginning ~15 UT on 9 July (see Figures 8a–8h and Table 1).

Similarly, a polar low evolving over Greenland at the same time likely also yielded frontal GWs. This caused localized strong surface flows north of the PMC Turbo location toward the south and SSE below winds near

Table 2
PMC Turbo Dynamics and Likely MLT Impacts

Date	Time (UT)	PMC event dynamics	Likely impacts
8 July	13–18	Weak small-scale MSD Largely small-scale GWs and KHI Few apparent instability events	Weak dynamics and instabilities suggest very weak MLT forcing
9 July	01–04	Weak small-scale MSD Largely small-scale GWs and KHI Few apparent instability events	Weak dynamics and instabilities suggest very weak MLT forcing
9 July	12–19	Weak GWs and small-scale KHI Weak initial instability intensities Instabilities increasing after ~15 UT Bores and many unknown features	Small initial energy and momentum inputs; expected increasing MLT forcing after ~15 UT
10 July	01:30–07:00 17:30–22:30	Strong GW breaking and instabilities Vortex ring evolutions and breakdown MSD evolutions including cusps Bores and SA dynamics Unknown features at large/small scales	Large energy and momentum inputs, strong instabilities, and implied MLT forcing
11 July	00:30–15:00	Large- and small-scale GWs, breaking Strong GW instability dynamics, vortex ring evolutions MSD event evolutions KHI, secondary instabilities, breakdown Filaments and unknown features	Large energy and momentum inputs, strong implied MLT forcing
11 July	21–24	Weaker GWs and instabilities GW fronts/bores and trailing instabilities Weaker MSD superpositions Small-scale KHI Unknown features at large and small scales	Likely small energy and momentum inputs, weak MLT forcing
12 July	11–18	Multiple small-scale KHI events MSD superpositions and weak instabilities SGW events and small-scale responses Small-scale filaments, unknown cause Large-scale KHI, GW breaking ~13–16 UT Multiple unknown dynamics, large/small	Mostly weak GW and KHI dynamics; likely weak and occasionally moderate/strong energy and momentum transport, MLT forcing
13 July	06–16	Multiple MSD events having complex instability structures Multiple small-scale KHI events Small- and large-scale SA dynamics Multiple GW fronts or bores and trailing instabilities	Largely weak to moderate GWs, KHI, and MSD; likely weak to moderate fluxes and MLT forcing

Note. GWs = gravity waves; KHI = Kelvin-Helmholtz instabilities; MLT = mesosphere and lower thermosphere; MSD = multiscale dynamics; PMC = polar mesospheric cloud; PMC Turbo = Polar Mesospheric Cloud Turbulence experiment; SA = self-acceleration; SGW = secondary GW; UT = universal time.

the tropopause that rotated from toward SW to toward SSE up to ~12 UT on 11 July (see Figures 8a–8d). These forcing and propagation conditions likely enabled mountain wave (MW) generation and propagation into the lower stratosphere at these times. A second evolving, but weaker, polar low and associated jet stream (not shown) likely contributed to GW generation after ~12 UT on 12 July over Northern Canada.

3.2. Stratospheric Fields and Implications

Winds above ~10 km were largely zonal (Figure 8i) and decreased above the stratopause at ~50 km (Figure 8j) from ~50 to ~30 m/s toward the west over this interval. An along-track $T'(z)$ cross section across Greenland (Figure 8k) from the ECMWF global model when PMC Turbo was at the blue dots shown in Figures 8a–8h suggests westward propagating GWs having horizontal wavelengths λ_h ~ 100 km and larger at ~10–30 km over Greenland and eastward propagating GWs at larger λ_h at ~35–65 km. The ECMWF model cannot resolve GW λ_h ~ 50 km and less but has shown an ability to describe GW generation due to orography and jet streams, though at smaller T' than measured during the Deep Propagating Gravity Wave Experiment (DEEPWAVE) program performed over New Zealand in 2014 (Fritts et al., 2016). GWs are expected to be underestimated by ECMWF due to increasing damping above ~30 km, suggesting larger amplitudes in

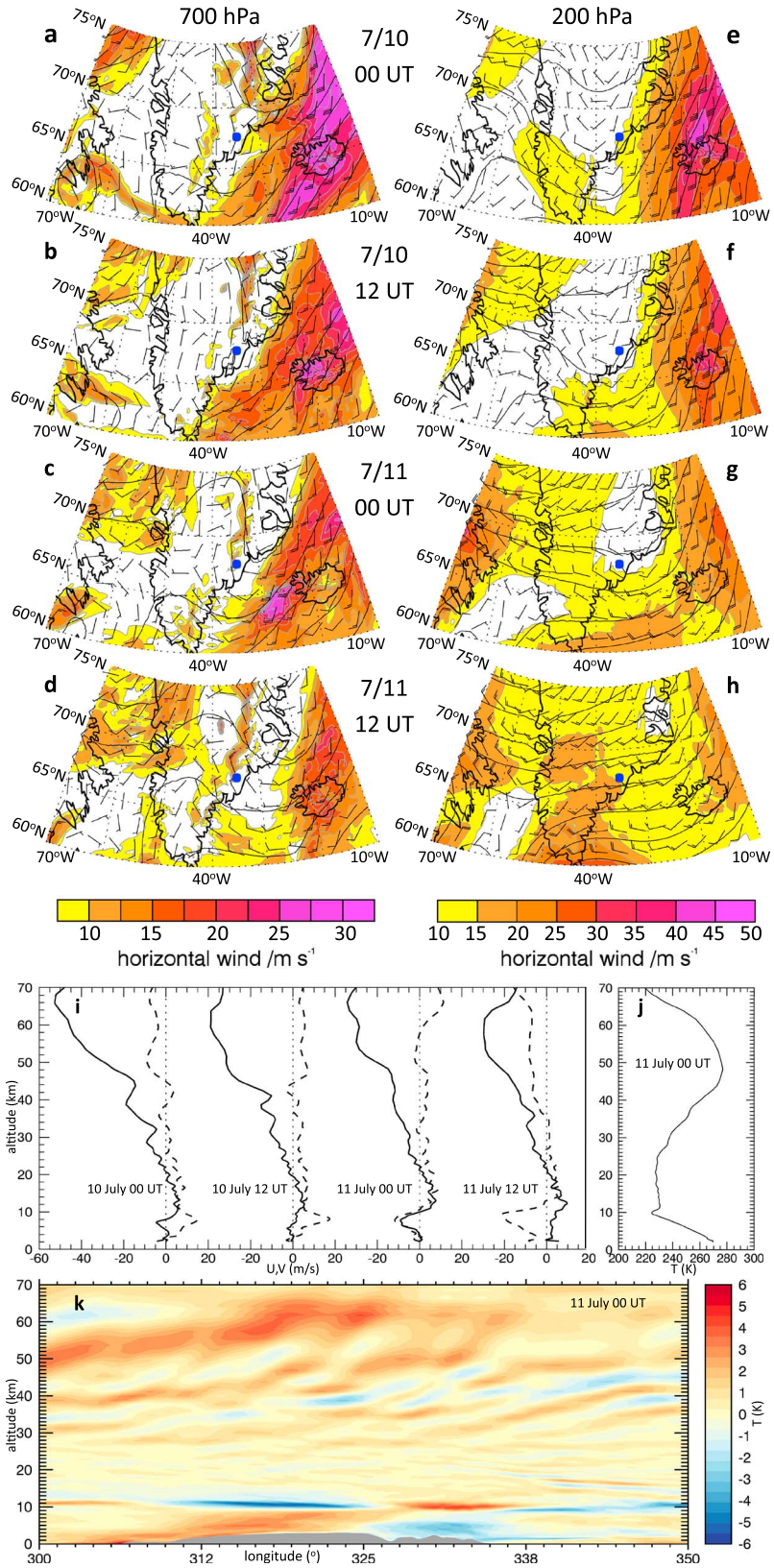

Figure 8. (a–h) ECMWF winds (colors and wind barbs) and geopotential heights (black lines) at 700 and 200 hPa, (i) 12-hourly mean winds from 0 to 70 km at four times, (j) a time-mean $T(z)$ on 11 July, and (k) a $T'(z)$ along-track cross section over Greenland at 00 UT on 11 July showing GWs from ~10–65 km.

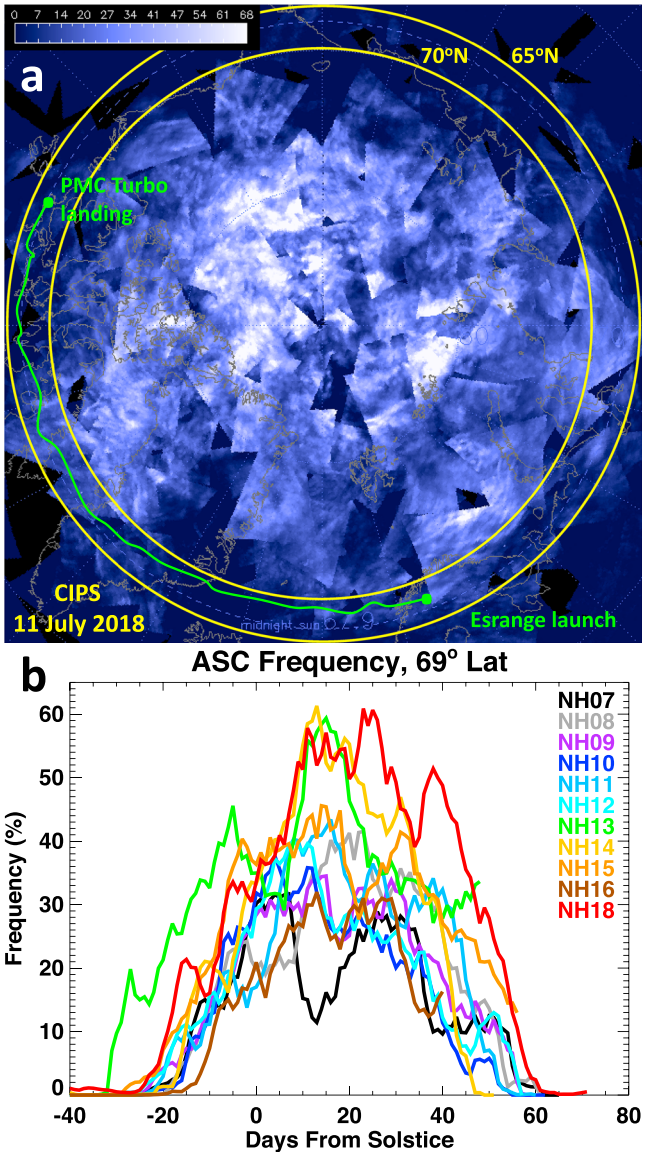

Figure 9. (a) CIPS PMC brightness poleward of 65°N on 11 July 2018 during the PMC Turbo flight and (b) intraseasonal and interannual variability of PMC occurrence at 69°N from 2007 to 2018.

reality than seen in Figure 8k. By comparison, BOLIDE $T'(z)$ below the PMC layer (Figure 6a) reveal apparent large-scale GWs extending to ~70°km and smaller GW scales above.

Implications of the ECMWF fields in Figure 8 are that there was likely strong GW generation by the jet stream off the eastern Greenland coast beginning earlier and extending into the interval shown and that there was likely strong, local generation of MWs able to propagate toward north and NW as the upper tropospheric wind field rotated in time. Upward propagation of MWs would have been confined to lower altitudes by the component wind reversals at ~10 km near 00 UT on July 11, but GWs arising due to jet stream generation (see Plougonven & Zhang, 2014) having significant phase speeds toward west or NW could have reached higher altitudes until approaching critical levels where the phase speed equals the mean wind along the GW propagation direction. Similarly, jet stream generation likely accounted for the larger-scale GWs having upward and eastward phase slopes seen in Figure 8j at ~25–60 km eastward of ~40°W at 00 UT on 11 July and for the large-scale upward and eastward propagating GWs seen by the lidar at higher altitudes somewhat thereafter in Figure 6a.

Where these various GWs were prevented from propagating to higher altitudes, they likely would have undergone breaking and instability dynamics such as seen in the PMC Turbo imaging discussed above. These dynamics would have resulted in the generation of additional SGWs at smaller and larger λ_h that readily propagated to higher and lower altitudes, until they suffered the same fate near their critical levels or until their amplitudes became sufficient to yield instabilities in the absence of critical levels (see Fritts and Alexander, 2003). Importantly, these SGWs would have been able to grow significantly in amplitude between the altitude of generation and the PMC altitude near 82 km. As an example, MWs breaking at ~10 km would have yielded SGWs that would have grown significantly in amplitude over an altitude range spanning approximately 10 scale heights (even accounting for horizontal dispersion) and would have exhibited their own breaking and instability dynamics where amplitude growth with increasing altitude and GW refraction by the background wind and temperature fields yielded large amplitudes. Indeed, it is likely that a significant fraction of the instability dynamics seen in the PMC layer is due to SGWs because of strong filtering of the primary GWs by the large-scale winds in the stratosphere and mesosphere.

4. CIPS Imaging and PMC Turbo Comparisons

4.1. CIPS Seasonal Variations

The Cloud Imaging and Particle Size (CIPS) instrument on the NASA Aeronomy of Ice in the Mesosphere (AIM) satellite has performed global observations of PMCs beginning prior to the 2007 Northern Hemisphere (NH) season. An example of the daily CIPS coverage during the PMC Turbo flight is shown in Figure 9a. Individual and composite images yield daily PMC occurrence frequencies above the detection threshold that have been applied in multiple studies of GW, planetary wave (PW), and tidal dynamics and statistics (see, as examples, Chandran et al., 2010; France et al., 2018; Merkel et al., 2009; Yue et al., 2014). The image in Figure 9a illustrates a number of features of general PMC distributions, among them (1) the brightest, nearly continuous responses at higher latitudes; (2) decreasing occurrence frequency and brightness at decreasing latitudes; (3) significant longitudinal variations in brightness at larger scales, suggesting systematic tidal and PW influences; (4) evidence of GWs at spatial scales varying from ~50 to ~500 km or larger; and (5) PMC voids that likely have dynamical causes but that are not understood at this time.

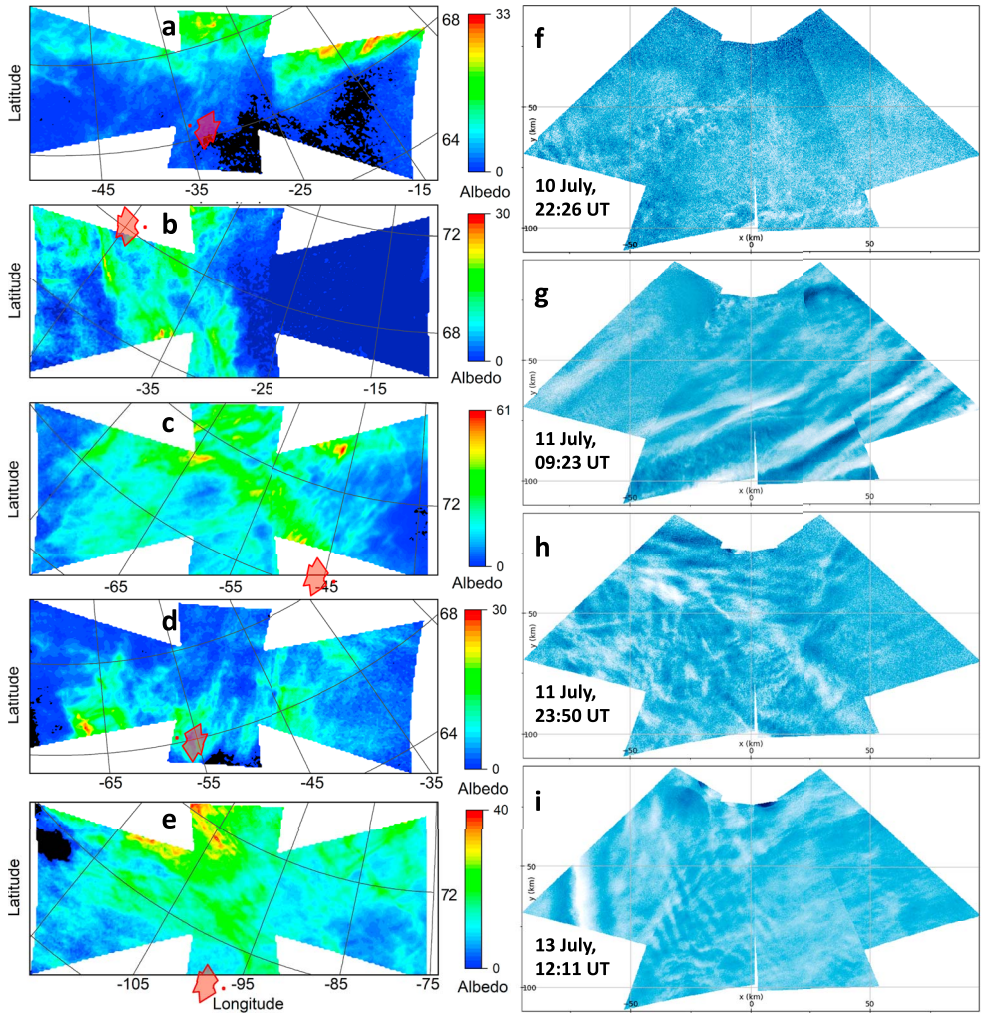

Figure 10. CIPS albedo images nearest the PMC Turbo balloon (a–e) at 22:26 UT on 10 July; 07:28, 09:23, and 23:50 UT on 11 July; and 12:11 UT on 13 July, on AIM orbits 61369, 61375, 61376, 61385, and 61408. PMC Turbo balloon and image locations are shown with red dots and wide fields of view (FOVs). (f–i) PMC Turbo wide-FOV images at the locations and times shown in a, c, d, and e.

PMC frequencies at 69°N for summers since 2007 are shown in Figure 9b. The different years reveal a common tendency for frequencies to peak within the month following summer solstice, apart from occasional later and smaller peaks in several seasons. All seasons exhibit significant multiday variations that are attributed to PW modulations of mesospheric temperatures having periods from ~2 to 30 days. These modulations accompany PW vertical motions and variable mean upwelling at PMC altitudes accompanying PW-mean flow interactions (France et al., 2018; Merkel et al., 2009).

The red line in Figure 9b shows the NH 2018 PMC season and reveals it to have been one of the more continuous and sustained annual responses, with a broad peak from ~1 to 16 July and the major occurrence extending from ~10 to 16 July, which spanned our PMC Turbo measurements.

4.2. CIPS and PMC Turbo Coincidences

During the PMC Turbo flight, the AIM satellite was in an orientation that resulted in CIPS composite images aligned with their long axes largely across rather than along the AIM flight track. As a result, CIPS imaging of PMCs provided only ~50% coverage along the flight track. Five CIPS images from 10 to 13 July coincident, or nearly coincident, with the PMC Turbo balloon locations are shown in Figures 10a–10e. Four wide-FOV PMC Turbo images at times coincident with CIPS PMCs in Figures 10a and 10c–10e are shown in

Figures 10f–10i. The AIM orbit was such that the majority of images near the PMC Turbo location at ~65–70°N were on ascending orbits (Figures 10a and 10d) approaching 00 UT or on descending orbits at ~8–12 UT hours later (Figures 10b, 10c, and 10e). These times largely coincided with intervals during which PMC Turbo observed weak or no PMCs due to the modulation of temperatures at ~80–85 km by the SDT, as discussed above. In all cases shown at the left in Figure 10, the CIPS albedo was ~0–20 at the PMC Turbo location, substantially below the peak values seen in the individual CIPS images and over the polar cap for all of 11 July in Figure 9a. Despite the low PMC brightness during these coincident images, the PMC imagers had sufficient sensitivity to reveal significant GW and instability dynamics at larger and smaller spatial scales in four of the five events (see Figures 10f–10i and and summaries of their environmental contexts in Table 1).

Only two coincident, fully overlapping, and two partially overlapping CIPS and PMC Turbo image pairs were possible over the PMC Turbo flight (see Figures 10a, 10b, 10d, and 10e). The image pair in Figures 10a and 10f exhibits weak PMC brightness and apparent instability features that are difficult to diagnose, while no PMC Turbo images were seen accompanying Figure 10b. However, CIPS did provide evidence of likely smaller-scale dynamics activity in the latter three cases.

Figure 10c shows apparent GW phase structures having λ_h ~ 50 km and smaller within ~100–200 km north and west of the PMC Turbo image. The image in Figure 10g indicates that these features extend to scales as small as λ_h ~ 10 km and provides some evidence of smaller-scale instabilities, especially at the upper and lower edges.

Figure 10d exhibits strong albedo variations that suggest the presence of GWs having λ_h ~ 30–300 km or larger, significant amplitudes, and a strong potential for instabilities where they interact with large-scale shears at PMC altitudes. The coincident PMC Turbo image in Figure 10h shows a complex GW field with embedded instability dynamics at smaller scales that are seen to exhibit rapid and strong transitions to turbulence in an image sequence about this time. BOLIDE data at this time in Figure 5d reveal a single, bright PMC layer exhibiting significant vertical excursions at observed periods of ~5–10 min, consistent with dynamics yielding strong local instabilities.

The CIPS image in Figure 10e exhibits not only less distinct larger-scale features but also evidence of GWs having λ_h ~ 100–300 km and larger, multiple orientations, and weaker amplitudes north and NE of the PMC Turbo image location. At, and extending ~100 km north of, the PMC Turbo image are CIPS albedo variations at scales of ~30 km or less. The character of these structures cannot be inferred from the CIPS imaging, but the corresponding PMC Turbo imaging around this image time reveals superposed GWs having λ_h ~ 15–30 km, with occasional larger GW amplitudes leading to local instabilities.

These examples suggest clear benefits of CIPS and PMC Turbo image comparisons, and subsequent PMC Turbo papers addressing specific dynamics sequences will explore several of these cases in greater detail.

5. PMC Turbo Event Imaging

5.1. Wide-FOV Images

Three PMC Turbo images from large-FOV cameras revealing some of the diversity of dynamics in regions of ~40–60 km in width are shown in Figure 11. Figure 11a shows what appears to be a GW front with trailing vortices, an intrusion, or most likely a mesospheric bore at 13:50 UT on 13 July, based on interpretations of similar imaging (Fechine et al., 2009; Fritts et al., 2017; Li et al., 2013; Miller et al., 2015; Narayanan et al., 2009; Smith et al., 2003; and references therein).

Figure 11b exhibits both initial "herringbone" instability structures along an apparent GW phase (upper right) and multiple small darker regions encircled partially or fully by brighter edges suggesting vortex rings, especially in the center and lower half of the image at 18:15 UT on 10 July (see modeling results in Fritts et al., 2017). The ring diameters are typically ~0.5–2 km, and their clustering in several regions resembles the cusp-like features seen from the EBEX stratospheric balloon and described by Miller et al. (2015) and Fritts et al. (2017).

Figure 11c shows interacting KH billows in greater detail than seen in Figure 3b at 13:35 UT on 12 July. Specific features include streamwise-aligned secondary instabilities, especially at the upper right, and

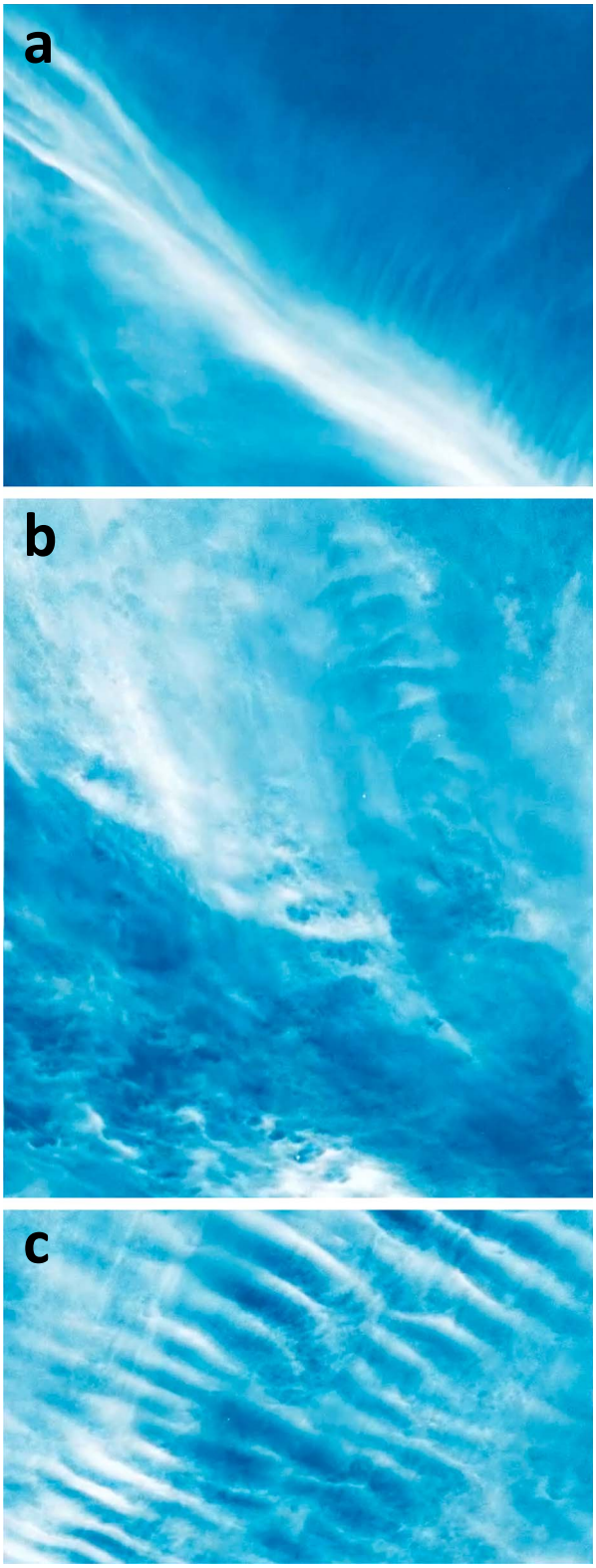

Figure 11. PMC Turbo ~45-km wide FOVs of diverse dynamics with (a) an apparent intrusion, (b) initial instability structures and small-scale vortex rings (top and bottom, respectively), and (c) KH billows undergoing interactions, instabilities, and merging.

regions of significant secondary instability dynamics where adjacent KH billows interact strongly, especially in the central part of the image.

5.2. Narrow-FOV Images

Examples of three instabilities contributing to GW breaking at different spatial scales seen at higher resolution are shown in Figure 12. All were obtained with Camera 3 and have widths of ~13 km at their respective locations. Figure 12a shows a succession of vortex rings lasting from 08:40 to 08:45 UT on 11 July and exhibiting streamwise vortex linkages between adjacent rings along the apparent GW propagation direction from lower right to upper left, as observed from the ground and stratosphere and modeled by Fritts et al. (2017). The vortex ring diameters in this case are ~2–4 km, suggesting a GW vertical wavelength exceeding ~5–10 km and low to moderate implied turbulence intensities (see Fritts et al., 2009b; Fritts et al., 2017). Lidar data at this time in Figure 5c reveal large vertical displacements consistent with GW overturning at these scales.

Figure 12b shows a single, very large-scale vortex ring at 05:50 UT on 11 July that remained coherent for more than 5 min, occurred during a very active period in close proximity to other vortex rings having comparable scales, and likely implies the strongest GW breaking and turbulence intensities inferred at any altitude to date. The vortex ring in this and other images in the series had a diameter of ~8 km, implying a large ε based on predictions by Fritts et al. (2017), given that $\varepsilon \sim \lambda_z^2$.

Figure 12c shows instability dynamics occurring from 09:05 to 09:11 UT on 11 July previously seen only in MSD modeling in cases where GW breaking appeared to be relatively weak. In these cases, the PMC fields suggest that the GW had λ_h ~ 3–4 km and was apparently strongly localized and modulated by another GW having a nearly orthogonal orientation. This led to apparent small-scale counterrotating vortices oriented between the two GW orientations but similar to those seen in the initial stages of weaker GW breaking at small λ_h and the outer portions of KH billows at small *Ri* and large *Re*. Importantly, this λ_h is far too small to have allowed this GW to have propagated from the troposphere, so it would have had to have been generated within the mesosphere.

More complete and quantitative analyses of these and other GW and instability events, and their correlations with potential sources and propagation environments, will be described in subsequent publications.

6. Discussion

As noted above, ground-based and limited stratospheric balloon PMC imaging studies have made valuable contributions to our understanding of GW structures and resulting instability dynamics in the mesosphere over many years (Baumgarten & Fritts, 2014; Dalin et al., 2010, 2019; Dubietis et al., 2011; Fritts et al., 2017; Witt, 1962). Extensive airglow observations at many sites and latitudes have also contributed to defining GW sources, scales, and climatologies and, more recently, in applications to smaller-scale instability dynamics (see Hecht, 2004; Hecht et al., 2014, 2018; Taylor, 1997; Yamada et al., 2001).

Previous ground-based studies employing lidars, radars, and/or PMC imaging have quantified other aspects of PMCs and the environments in which they occur. Multiple lidar studies have revealed PMC vertical

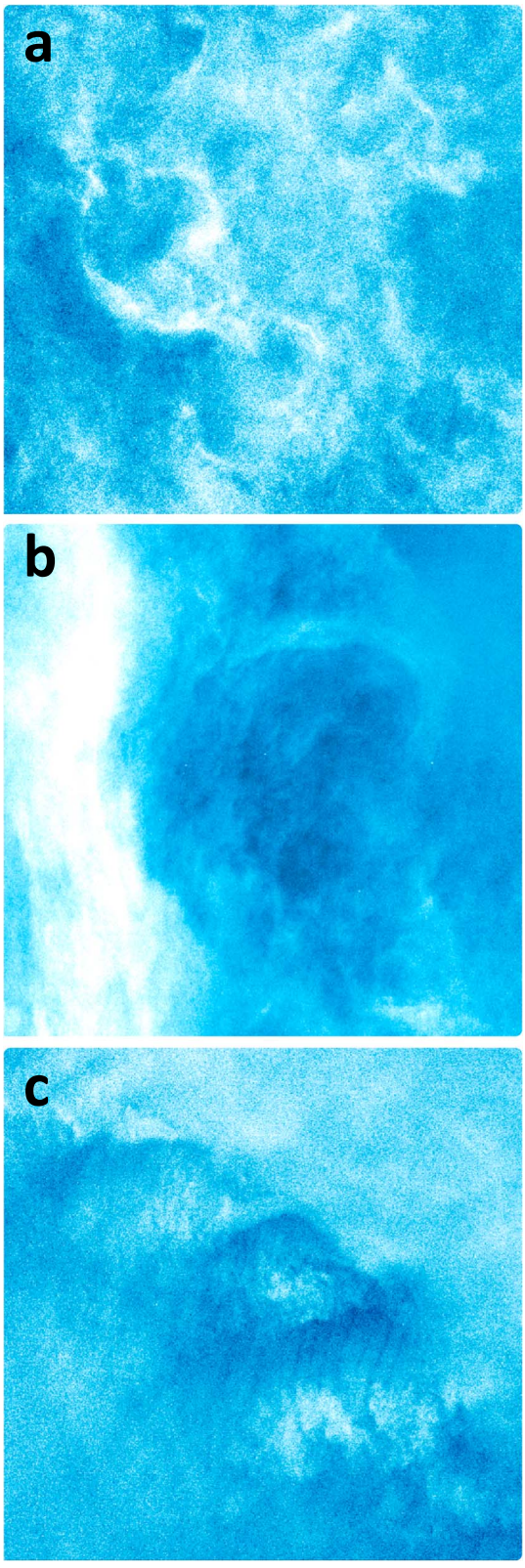

Figure 12. As in Figure 11 for narrow field-of-view images. (a) Medium- and (b) large-scale vortex rings and (c) a previously unseen initial instability form for a very small-scale λ_h gravity wave all observed on 11 July.

displacements implying GW amplitudes and periods, relations of PMCs with specific phases of GW temperature perturbations, the frequent occurrence of multiple, closely spaced brightness (or backscatter) maxima, and evidence for very thin PMC layers enabling especially high sensitivity to small-scale instability and turbulence structures (Baumgarten et al., 2012; Collins et al., 2003, 2009; Fiedler et al., 2005, 2011; Fritts et al., 2017). Other lidar studies explored the relation between MWs and more general GW amplitudes and PMC brightness, generally confirming model predictions of a negative correlation among these quantities (Gerrard et al., 1998, 2004; Thayer et al., 2003).

Newer PMC imaging by CIPS has likewise contributed to GW studies at polar summer latitudes and enabled correlative studies with ground-based measurements (Baumgarten et al., 2012; Chandran et al., 2009, 2010; Taylor et al., 2011). Among the key findings by CIPS observations that is potentially of relevance to PMC Turbo studies are occurrences of ice voids that can occur from relatively small λ_h ~50- to ~1,000-km scales (Thurairajah et al., 2013). These appear to be due to local temperature maxima and may be clues to important larger-scale dynamics at these altitudes, but the causes of these voids are not understood at present.

Our PMC Turbo observations and current analyses have a more specific focus on GW instability dynamics for several reasons. They are central to, and contribute to understanding of, GW energy and momentum deposition in the MLT, at lower altitudes, and in other geophysical fluids. They play key roles in mixing and transport from the surface into the thermosphere, which depend on instability character and are poorly understood at this time. As such, they underpin the need for improved parameterizations of these dynamics in global research, weather, and climate models throughout the atmosphere. The unique ability to observe these dynamics in spectacular detail in the PMC layer makes these regions likely the best place on Earth to study these dynamics of wide geophysical relevance.

The importance and relevance of instability dynamics to GW and turbulence parameterizations imply a need for a more comprehensive understanding of the variability of GW instabilities with tropospheric weather, GW propagation environments, altitude, geography, season, and specific GW responses. Both PMC and airglow imaging can contribute, as noted above, but there are very few observations available from which to assemble useful climatologies at this time. The strongest responses accompany GWs having the largest λ_z and ω_i, hence the largest energy and momentum fluxes and deposition. However, the largest events are infrequent, based on observations to date, and more frequent weaker events surely also have important, and perhaps different, effects. As an example, we expect quite different implications for mixing and transport accompanying GW breaking and KHI, based on modeling studies of idealized flows.

PMC imaging at northern and southern polar latitudes has revealed similar instability dynamics and scales, and airglow imaging has revealed similar instability dynamics at comparable scales at lower latitudes in some cases (Pautet et al., 2016, Figure 3). Other data, such as in situ rocket measurements of turbulence intensities during summer and winter over Northern Norway by Lübken (1997), provide useful

insights into seasonal variations. However, there are insufficient observations of instability events from which to discern the statistical dependence of spatial and temporal variability on background atmospheric parameters. PMC observations have the potential to contribute to such a climatology at a specific season and altitude, but airglow data will be needed to address their statistics at other seasons and lower latitudes. In contrast, satellite characterization of GW variances spans all latitudes and seasons and large altitude ranges but is largely insensitive to the smaller-λ_h and larger-ω_i GWs expected to contribute most to energy and momentum deposition at all altitudes (Fritts, Vosper, et al., 2018; Preusse et al., 2008).

Importantly for our purposes, PMC observations continue to provide the greatest sensitivity to small-scale instability dynamics leading to turbulence, which is the primary focus of our PMC Turbo analyses. These capabilities, and viewing from the stratosphere, have enabled a number of new instability observations not previously seen in PMC or airglow imaging from the ground. New instability observations identified to date include the first detections of (1) KH billows exhibiting secondary KHI, (2) multiple cases of KH billow interactions, (3) superposed strong KHI and larger-scale vortex rings, (4) the largest vortex rings seen to date, and (5) strong apparent modulation of GW instability intensities seen in PMCs by underlying weather.

Given the initial PMC Turbo results described above, we anticipate that additional PMC Turbo studies will benefit from the following new analysis capabilities relative to previous ground-based and EBEX PMC imaging studies:

1. Viewing closer to zenith than in typical ground-based imaging will largely avoid uncertainties in characterizing horizontal primary and secondary instability scales.
2. PMC Turbo imaging at high spatial and temporal resolution with camera FOVs varying from ~13- to ~30-km widths at smaller off-zenith angles, and a composite FOV of ~80 × 120 km, has captured dynamics sequences not resolved spatially by ground-based imaging and not imaged completely, nor resolved temporally, by EBEX star cameras.
3. Near-vertical PMC imaging and lidar profiling will allow a clear distinction between features varying in the horizontal and vertical, which has been a challenge in previous imaging at low elevation angles.
4. One nearly continuous 24-hr PMC imaging interval may enable exploration of differing dynamical responses and/or orientations to differing SDT phases and wind shears.
5. The ~5.5-day PMC Turbo flight spanning various topography and tropospheric weather will hopefully allow more detailed exploration of their influences on GW and instability dynamics.
6. Correlative analyses with CIPS may enable exploration of the dynamical causes of larger-scale responses, among them PMC voids at larger and smaller scales.

7. Summary and Conclusions

The PMC Turbo stratospheric balloon flight from Esrange, Sweden, to Northern Canada was an alternate to our initially intended flight from McMurdo Station, Antarctica, that was anticipated to include two circuits around the polar vortex over Antarctica and that would have been ~2–4 times as long. The Esrange launch was offered by NASA when it became clear that PMC Turbo would be unable to fly from McMurdo during the 2017–2018 austral summer. Our flight nevertheless achieved significant PMC imaging at an optimal time during the 2018 NH summer season. Hence, we are confident that our team will be able to perform many valuable analyses, given what we have learned of the quality of the data set, and the diversity of dynamics captured, in our initial assessments of the data.

Werner Heisenberg was reported to have said “When I meet God, I am going to ask him two questions: Why relativity? And why turbulence? I really believe he will have an answer for the first”. PMC Turbo imaging and analyses will not answer Heisenberg's “Why turbulence?” But we believe that PMC Turbo analyses and related modeling will make significant contributions to answering how, from what sources, at what scales, by what mechanisms, and with what intensities turbulence arises in the mesosphere, and by extrapolation in other geophysical fluids. These efforts will hopefully also help determine what GW sources, scales, and propagation environments play the major roles in forcing the MLT.

Acknowledgments

Research described here was supported under NASA and NSF grants cited in GEMS. This project also received funding from the German Aerospace Center (DLR) for construction, integration, and operation of the Rayleigh lidar and subsequent data analyses. We thank three reviewers for valuable comments on the manuscript. Access to ECMWF data was possible through the special project HALO Mission Support System. Links to data required to replicate all PMC Turbo images and other figures in this paper are available in the supporting information.

References

Andreassen, Ø., Hvidsten, P. Ø., Fritts, D. C., & Arendt, S. (1998). Vorticity dynamics in a breaking gravity wave. Part 1. Initial instability evolution. *Journal of Fluid Mechanics*, *367*, 27–46. https://doi.org/10.1017/S0022112098001645

Baumgarten, G., Chandran, A., Fiedler, J., Hoffmann, P., Kaifler, N., Lumpe, J., et al. (2012). On the horizontal and temporal structure of noctilucent clouds as observed by satellite and lidar at ALOMAR (69N). *Geophysical Research Letters*, *39*, L01803. https://doi.org/10.1029/2011GL049935

Baumgarten, G., & Fritts, D. C. (2014). Quantifying Kelvin-Helmholtz instability dynamics observed in noctilucent clouds: 1. Methods and observations. *Journal of Geophysical Research: Atmospheres*, *119*, 9324–9337. https://doi.org/10.1002/2014JD021832

Bossert, K., Kruse, C. G., Heale, C. J., Fritts, D. C., Williams, B. P., Snively, J. B., et al. (2017). Secondary gravity wave generation over New Zealand during the DEEPWAVE campaign. *Journal of Geophysical Research: Atmospheres*, *122*, 7834–7850. https://doi.org/10.1002/2016JD026079

Bretherton, F. P. (1969). Momentum transport by gravity waves. *Quarterly Journal of the Royal Meteorological Society*, *95*(404), 213–243. https://doi.org/10.1002/qj.49709540402

Chandran, A., Rusch, D. W., Merkel, A. W., Palo, S. E., Thomas, G. E., Taylor, M. J., et al. (2010). Polar mesospheric cloud structures observed from the cloud imaging and particle size experiment on the Aeronomy of Ice in the Mesosphere spacecraft: Atmospheric gravity waves as drivers for longitudinal variability in polar mesospheric cloud occurrence. *Journal of Geophysical Research*, *115*, D13102. https://doi.org/10.1029/2009JD013185

Chandran, A., Rusch, D. W., Palo, S. E., Thomas, G. E., & Taylor, M. J. (2009). Gravity wave observations in the summertime polar mesosphere from the Cloud Imaging and Particle Size (CIPS) experiment on the AIM spacecraft. *Journal of Atmospheric and Solar - Terrestrial Physics*, *71*(3-4), 392–400. https://doi.org/10.1016/j.jastp.2008.09.041

Collins, R. L., Kelley, M. C., Nicolls, M. J., Ramos, C., Hou, T., Stern, T. E., et al. (2003). Simultaneous lidar observations of a noctilucent cloud and an internal wave in the polar mesosphere. *Journal of Geophysical Research*, *108*(D8), 8435. https://doi.org/10.1029/2002JD002427

Collins, R. L., Taylor, M. J., Nielsen, K., Mizutani, K., Murayama, Y., Sakanoi, K., & DeLand, M. T. (2009). Noctilucent cloud in the western Arctic in 2005: Simultaneous lidar and camera observations and analysis. *Journal of Atmospheric and Solar - Terrestrial Physics*, *71*(3-4), 446–452. https://doi.org/10.1016/j.jastp.2008.09.044

Dalin, P., Pertsev, N., Frandsen, S., Hansen, O., Andersen, H., Dubietis, A., & Balciunas, R. (2010). A case study of the evolution of a Kelvin-Helmholtz wave and turbulence in noctilucent clouds. *Journal of Atmospheric and Solar - Terrestrial Physics*, *72*(14-15), 1129–1138. https://doi.org/10.1016/j.jastp.2010.06.011

Dalin, P., Pertsev, N., Perminov, V., Efremov, D., & Romejko, V. (2019). Looking at "night-shining" clouds from the stratosphere. *Eos*, *100*. https://doi.org/10.1029/2019EO118439

Dosser, H. V., & Sutherland, B. R. (2011). Weakly nonlinear non-Boussinesq internal gravity wavepackets. *Physica D*, *240*(3), 346–356. https://doi.org/10.1016/j.physd.2010.09.008

Dubietis, A., Dalin, P., Balčiūnas, R., Černis, K., Pertsev, N., Sukhodoev, V., et al. (2011). Noctilucent clouds: Modern ground-based photographic observations by a digital camera network. *Applied Optics*, *50*(28). https://doi.org/10.1364/AO.50.000F72

Eaton, F., Mclaughlin, S. A., & Hines, J. R. (1995). A new frequency modulated continuous wave radar for studying planetary boundary layer morphology. *Radio Science*, *30*(1), 75–88. https://doi.org/10.1029/94RS01937

Eckermann, S. D., Broutman, D., Ma, J., Doyle, J. D., Pautet, P.-D., Taylor, M. J., et al. (2016). Dynamics of orographic gravity waves observed in the mesosphere over the Auckland Islands during the Deep Propagating Gravity Wave Experiment (DEEPWAVE). *Journal of the Atmospheric Sciences*, *73*(10), 3855–3876. https://doi.org/10.1175/JAS-D-16-0059.1

Fechine, J., Wrasse, C. M., Takahashi, H., Medeiros, A. F., Batista, P. P., Clemesha, B. R., et al. (2009). First observation of an undular mesospheric bore in a Doppler duct. *Annales Geophysicae*, *27*(4), 1399–1406. https://doi.org/10.5194/angeo-27-1399-2009

Fiedler, J., Baumgarten, G., Berger, U., Hoffman, P., Kaifler, N., & Lubken, F.-J. (2011). NLC and the background atmosphere above ALOMAR. *Atmospheric Chemistry and Physics*, *11*(12), 5701–5717. https://doi.org/10.5194/acp-11-5701-2011

Fiedler, J., Baumgarten, G., & Von Cossart, G. (2005). Mean diurnal variations of noctilucent clouds during 7 years of lidar observations at ALOMAR. *Annales Geophysicae*, *23*(4), 1175–1181. https://doi.org/10.5194/angeo-23-1175-2005

France, J. A., Randall, C. E., Lieberman, R. S., Harvey, V. L., Eckermann, S. D., Siskind, D. E., et al. (2018). Local and remote planetary wave effects on polar mesospheric clouds in the Northern Hemisphere in 2014. *Journal of Geophysical Research: Atmospheres*, *123*, 5149–5162. https://doi.org/10.1029/2017JD028224

Franke, P. M., & Collins, R. L. (2003). Evidence of gravity wave breaking in lidar data from the mesopause region. *Geophysical Research Letters*, *30*(4), 1155. https://doi.org/10.1029/2001GL014477

Fritts, D. C., & Alexander, M. J. (2003). Gravity dynamics and effects in the middle atmosphere. *Reviews of Geophysics*, *41*(1), 1003. https://doi.org.10.1029/2001RG000106

Fritts, D. C., Arendt, S., & Andreassen, O. (1998). Vorticity dynamics in a breaking internal gravity wave. Part 2. Vortex interactions and transition to turbulence. *Journal of Fluid Mechanics*, *367*, 47–65. https://doi.org/10.1017/S0022112098001633

Fritts, D. C., Baumgarten, G., Wan, K., Werne, J. A., & Lund, T. (2014). Quantifying Kelvin-Helmholtz instability dynamics observed in noctilucent clouds: 2. Modeling and interpretation of observations. *Journal of Geophysical Research: Atmospheres*, *119*, 9324–9337. https://doi.org/10.1002/2014JD021832

Fritts, D. C., Isler, J. R., & Andreassen, Ø. (1994). Gravity wave breaking in two and three dimensions: 2. Three-dimensional evolution and instability structure. *Journal of Geophysical Research*, *99*(D4), 8109–8123. https://doi.org/10.1029/93JD03436

Fritts, D. C., Isler, J. R., Thomas, G. E., & Andreassen, Ø. (1993). Wave breaking signatures in noctilucent clouds. *Geophysical Research Letters*, *20*(19), 2039–2042. https://doi.org/10.1029/93GL01982

Fritts, D. C., Laughman, B., Lund, T. S., & Snively, J. B. (2015). Self-acceleration and instability of gravity wave packets: 1. Effects of temporal localization. *Journal of Geophysical Research: Atmospheres*, *120*, 8783–8803. https://doi.org/10.1002/2015JD023363

Fritts, D. C., Laughman, B., Wang, L., Lund, T., & Collins, R. L. (2018). Gravity wave dynamics in a mesospheric inversion layer: 1. Reflection, trapping, and instability dynamics. *Journal of Geophysical Research: Atmospheres*., accepted 14 Sept, *123*, 626–648. https://doi.org/10.1002/2017JD027440

Fritts, D. C., & Rastogi, P. K. (1985). Convective and dynamical instabilities due to gravity wave motions in the lower and middle atmosphere: Theory and observations. *Radio Science*, *20*(6), 1247–1277. https://doi.org/10.1029/RS020i006p01247

Fritts, D. C., Vosper, S. B., Williams, B. P., Bossert, K., Plane, J. M. C., Taylor, M. J., et al. (2018). Large-amplitude mountain waves in the mesosphere accompanying weak cross-mountain flow during DEEPWAVE Research Flight RF22. *Journal of Geophysical Research: Atmospheres*, *123*, 9992–10,022. https://doi.org/10.1029/2017JD028250

Fritts, D. C., Wan, K., Werne, J., Lund, T., & Hecht, J. H. (2014). Modeling influences of Kelvin-Helmholtz instability dynamics on airglow. *Journal of Geophysical Research: Atmospheres*, *119*, 8858–8871. https://doi.org/10.1002/2014JD021737

Fritts, D. C., Wang, L., Baumgarten, G., Miller, A. D., Geller, M. A., Jones, G., et al. (2017). High-resolution observations and modeling of turbulence sources, structures, and intensities in the upper mesosphere. *Journal of Atmospheric and Solar - Terrestrial Physics*, *162*, 57–78. https://doi.org/10.1016/j.jastp.2016.11.006

Fritts, D. C., Wang, L., Geller, M. A., Lawrence, D. A., Werne, J., & Balsley, B. B. (2016). Numerical modeling of multi-scale dynamics at a high Reynolds number: Instabilities, turbulence, and an assessment of Ozmidov and Thorpe scales. *Journal of the Atmospheric Sciences*, *73*(2), 555–578. https://doi.org/10.1175/JAS-D-14-0343.1

Fritts, D. C., Wang, L., Laughman, B., Lund, T., & Collins, R. L. (2018). Gravity wave dynamics in a mesospheric inversion layer: 2. Instabilities, turbulence, fluxes, and mixing. *Journal of Geophysical Research: Atmospheres*, *123*, 649–670. https://doi.org/10.1002/2017JD027442

Fritts, D. C., Wang, L., & Werne, J. (2013). Gravity wave–fine structure interactions. Part 1: Influences of fine structure form and orientation on flow evolution and instability. *Journal of the Atmospheric Sciences*, *70*(12), 3710–3734. https://doi.org/10.1175/JAS-D-13-055.1

Fritts, D. C., Wang, L., Werne, J., Lund, T., & Wan, K. (2009a). Gravity wave instability dynamics at high Reynolds numbers. Part I: Wave field evolution at large amplitudes and high frequencies. *Journal of the Atmospheric Sciences*, *66*(5), 1126–1148. https://doi.org/10.1175/2008JAS2726.1

Fritts, D. C., Wang, L., Werne, J., Lund, T., & Wan, K. (2009b). Gravity wave instability dynamics at high Reynolds numbers. Part II: Turbulence evolution, structure, and anisotropy. *Journal of the Atmospheric Sciences*, *66*(5), 1149–1171. https://doi.org/10.1175/2008JAS2727.1

Gerrard, A. J., Kane, T. J., & Thayer, J. P. (1998). Noctilucent clouds and wave dynamics: Observations at Sondrestrom, Greenland. *Geophysical Research Letters*, *25*(15), 2817–2820. https://doi.org/10.1029/98GL02107

Gerrard, A. J., Kane, T. J., Thayer, J. P., & Eckermann, S. D. (2004). Concerning the upper stratospheric gravity wave and mesospheric cloud relationship over Sondrestrom, Greenland. *Journal of Atmospheric and Solar - Terrestrial Physics*, *66*(3-4), 229–240. https://doi.org/10.1016/j.jastp.2003.12.005

Heale, C. J., Bossert, K., Snively, J. B., Fritts, D. C., Pautet, P.-D., & Taylor, M. J. (2017). Numerical modeling of a multiscale gravity wave event and its airglow signatures over Mount Cook, New Zealand, during the DEEPWAVE campaign. *Journal of Geophysical Research: Atmospheres*, *122*, 846–860. https://doi.org/10.1002/2016JD025700

Hecht, J. H. (2004). Instability layers and airglow imaging. *Reviews of Geophysics*, *42*, RG1001. https://doi.org/10.1029/2003RG000131

Hecht, J. H., Fritts, D. C., Wang, L., Gelinas, L. J., Rudy, R. J., Walterscheid, R. L., & Franke, S. J. (2018). Observations of the breakdown of mountain waves over the Andes Lidar Observatory at Cerro Pachon on 8/9 July 2012. *Journal of Geophysical Research: Atmospheres*, *123*, 276–299. https://doi.org/10.1002/2017JD027303

Hecht, J. H., Liu, A. Z., Walterscheid, R. L., & Rudy, R. J. (2005). Maui Mesosphere and Lower Thermosphere (Maui MALT) observations of the evolution of Kelvin-Helmholtz billows formed near 86 km altitude. *Journal of Geophysical Research*, *110*, D09S10. https://doi.org/10.1029/2003JD003908

Hecht, J. H., Walterscheid, R. L., Fritts, D. C., Isler, J. R., Senft, D. C., Gardner, C. S., & Franke, S. J. (1997). Wave breaking signatures in OH airglow and sodium densities and temperatures 1. Airglow imaging, Na lidar, and MF radar observations. *Journal of Geophysical Research*, *102*(D6), 6655–6668. https://doi.org/10.1029/96JD02619

Hecht, J. H., Wan, K., Gelinas, L. J., Fritts, D. C., Walterscheid, R. L., Franke, S. J., et al. (2014). The lifecycle of instability features measured from the Andes Lidar Observatory over Cerro Pachon on March 24, 2012. *Journal of Geophysical Research: Atmospheres*, *119*, 8872–8898. https://doi.org/10.1002/2014JD021726

Holton, J. R. (1983). The influence of gravity wave breaking on the general circulation of the middle atmosphere. *Journal of the Atmospheric Sciences*, *40*(10), 2497–2507. https://doi.org/10.1175/1520-0469(1983)040<2497:TIOGWB>2.0.CO;2

Kaifler, B., Kaifler, N., Ehard, B., Dörnbrack, A., Rapp, M., & Fritts, D. C. (2015). Influences of source conditions on mountain wave penetration into the stratosphere and mesosphere. *Geophysical Research Letters*, *42*, 9488–9494. https://doi.org/10.1002/2015GL066465

Lehmacher, G. A., Guo, L., Kudeki, E., Reyes, P. M., Akgiray, A., & Chau, J. L. (2007). High resolution observations of mesospheric layers with the Jicamarca VHF radar. *Advances in Space Research*, *40*(6), 734–743. https://doi.org/10.1016/j.asr.2007.05.059

Lelong, M.-P., & Dunkerton, T. J. (1998a). Inertia–gravity wave breaking in three dimensions. Part I: Convectively stable waves. *Journal of the Atmospheric Sciences*, *55*(15), 2473–2488. https://doi.org/10.1175/1520-0469(1998)055<2473:IGWBIT>2.0.CO;2

Lelong, M.-P., & Dunkerton, T. J. (1998b). Inertia–gravity wave breaking in three dimensions. Part II: Convectively unstable waves. *Journal of the Atmospheric Sciences*, *55*(15), 2489–2501. https://doi.org/10.1175/1520-0469(1998)055<2489:IGWBIT>2.0.CO;2

Li, Q., Xu, J., Yue, J., Liu, X., Yuan, W., Ning, B., et al. (2013). Investigation of a mesospheric bore event over northern China. *Annales Geophysicae*, *31*(3), 409–418. https://doi.org/10.5194/angeo-31-409-2013

Lilly, D. K. (1978). A severe downslope windstorm and aircraft turbulence induced by a mountain wave. *Journal of the Atmospheric Sciences*, *35*(1), 59–77. https://doi.org/10.1175/1520-0469(1978)035<0059:ASDWAA>2.0.CO;2

Lilly, D. K., & Kennedy, P. J. (1973). Observations of a stationary mountain wave and its associated momentum flux and energy dissipation. *Journal of the Atmospheric Sciences*, *30*(6), 1135–1152. https://doi.org/10.1175/1520-0469(1973)030<1135:OOASMW>2.0.CO;2

Lindzen, R. S. (1981). Turbulence and stress owing to gravity wave and tidal breakdown. *Journal of Geophysical Research*, *86*(C10), 9707–9714. https://doi.org/10.1029/JC086iC10p09707

Lombard, P. N., & Riley, J. J. (1996). Instability and breakdown of internal gravity waves. I. Linear stability analysis. *Physics of Fluids*, *8*(12), 3271–3287. https://doi.org/10.1063/1.869117

Lübken, F.-J. (1997). Seasonal variation of turbulent energy dissipation rates at high latitudes as determined by in situ measurements of neutral density fluctuations. *Journal of Geophysical Research*, *102*(D12), 13,441–13,456. https://doi.org/10.1029/97JD00853

Merkel, A. W., Rusch, D. W., Palo, S. E., Russell, J. M. III, & Bailey, S. M. (2009). Mesospheric planetary wave effects on global PMC variability inferred from AIM–CIPS and TIMED–SABER for the northern summer 2007 PMC season. *Journal of Atmospheric and Solar - Terrestrial Physics*, *71*(3-4), 381–391. https://doi.org/10.1016/j.jastp.2008.12.001

Miller, A. D., Fritts, D. C., Chapman, D., Jones, G., Limon, M., Araujo, D., et al. (2015). Stratospheric imaging of noctilucent clouds: A new window on small-scale atmospheric dynamics. *Geophysical Research Letters*, *42*, 6058–6065. https://doi.org/10.1002/2015GL064758

Narayanan, V. L., Gurubaran, S., & Emperumal, K. (2009). A case study of a mesospheric bore event observed with an all-sky airglow imager at Tirunelveli (8.7°N). *Journal of Geophysical Research*, *114*, D08114. https://doi.org/10.1029/2008JD010602

Pautet, P.-D., Taylor, M. J., Fritts, D. C., Bossert, K., Williams, B. P., Broutman, D., et al. (2016). Large-amplitude mesospheric response to an orographic wave generated over the Southern Ocean Auckland Islands (50.7S) during the DEEPWAVE project. *Journal of Geophysical Research: Atmospheres*, *121*, 1431–1441. https://doi.org.10.1002/2015JD024336

Pavelin, E., Whiteway, J. A., & Vaughan, G. (2001). Observations of gravity wave breaking in the lowermost stratosphere. *Journal of Geophysical Research*, *104*(D6), 51,763–51,769. https://doi.org/10.1029/2000JD900480

Pfrommer, T., Hickson, P., & She, C.-Y. (2009). A large-aperture sodium fluorescence lidar with very high resolution for mesopause dynamics and adaptive optics studies. *Geophysical Research Letters*, *36*, L15831. https://doi.org/10.1029/2009GL038802

Plougonven, R., & Zhang, F. (2014). Internal gravity waves from atmospheric jets and fronts. *Reviews of Geophysics*, *52*, 33–76. https://doi.org.10.1002/2012RG000419

Preusse, P., Eckerman, S. D., & Ern, M. (2008). Transparency of the atmosphere to short horizontal wavelength gravity waves. *Journal of Geophysical Research*, *113*, D24104. https://doi.org/10.1029/2007JD009682

Smith, S. M., Taylor, M. J., Swenson, G. R., She, C.-Y., Hocking, W., Baumgardner, J., & Mendillo, M. (2003). A multidiagnostic investigation of the mesospheric bore phenomenon. *Journal of Geophysical Research*, *108*(A2), 1083. https://doi.org/10.1029/2002JA009500

Sonmor, L. J., & Klaassen, G. P. (1997). Toward a unified theory of gravity wave stability. *Journal of the Atmospheric Sciences*, *54*(22), 2655–2680. https://doi.org/10.1175/1520-0469(1997)054<2655:TAUTOG>2.0.CO;2

Staquet, C., & Sommeria, J. (2002). Internal gravity waves: From instabilities to turbulence. *Annual Review of Fluid Mechanics*, *34*(1), 559–593. https://doi.org/10.1146/annurev.fluid.34.090601.130953

Stevens, M. H., Lieberman, R. S., Siskind, D. E., McCormack, J. P., Hervig, M. E., & Englert, C. R. (2017). Periodicities of polar mesospheric clouds inferred from a meteorological analysis and forecast system. *Journal of Geophysical Research: Atmospheres*, *122*, 4508–4527. https://doi.org/10.1002/2016JD025349

Stober, G., Sommer, S., Schult, C., Latteck, R., & Chau, J. L. (2018). Observation of Kelvin–Helmholtz instabilities and gravity waves in the summer mesopause above Andenes in Northern Norway. *Atmospheric Chemistry and Physics*, *18*(9), 6721–6732. https://doi.org/10.5194/acp-18-6721-2018

Sutherland, B. R. (2001). Finite-amplitude internal wavepacket dispersion and breaking. *Journal of Fluid Mechanics*, *429*, 343–380. https://doi.org/10.1017/S0022112000002846

Sutherland, B. R. (2006). Internal wave instability: Wave-wave versus wave-induced mean flow interactions. *Physics of Fluids*, *18*(7), 074107. https://doi.org/10.1063/1.2219102

Swenson, G. R., & Mende, S. B. (1994). OH emission and gravity waves (including a breaking wave) in all-sky imagery from Bear Lake, UT. *Geophysical Research Letters*, *21*(20), 2239–2242. https://doi.org/10.1029/94GL02112

Taylor, M. J. (1997). A review of advances in imaging techniques for measuring short period gravity waves in the mesosphere and lower thermosphere. *Advances in Space Research*, *19*(4), 667–676. https://doi.org/10.1016/S0273-1177(97)00161-0

Taylor, M. J., Pautet, P.-D., Zhao, Y., Randall, C. E., Lumpe, J., Bailey, S. M., et al. (2011). High-latitude gravity wave measurements in noctilucent clouds and polar mesospheric clouds. In M. Abdu, & D. Pancheva (Eds.), *Aeronomy of the Earth's atmosphere and ionosphere. IAGA Special Sopron Book Series* (Vol. *2*, pp. 93–105). Dordrecht: Springer. https://doi.org/10.1007/978-94-007-0326-1_7

Thayer, J. P., Rapp, M., Gerrard, A. J., Gudmundsson, E., & Kane, T. J. (2003). Gravity-wave influences on Arctic mesospheric clouds as determined by a Rayleigh lidar at Sondrestrom, Greenland. *Journal of Geophysical Research*, *108*(D8), 8449. https://doi.org/10.1029/2002JD002363

Thorpe, S. A. (1973a). Experiments on instability and turbulence in a stratified shear flow. *Journal of Fluid Mechanics*, *61*(04), 731–751. https://doi.org/10.1017/S0022112073000911

Thorpe, S. A. (1973b). Turbulence in stably stratified fluids: A review of laboratory experiments. *Boundary Layer Meteorology*, *5*(1-2), 95–119 . https://doi.org/10.1007/BF02188314

Thorpe, S. A. (1977). Turbulence and mixing in a Scottish loch. *Philosophical Transactions of the Royal Society of London. Series A, Mathematical and Physical Sciences*, *A286*, 125–181. https://doi.org/10.1098/rsta.1977.0112

Thorpe, S. A. (1987). Transitional phenomena and the development of turbulence in stratified fluids: A review. *Journal of Geophysical Research*, *92*(C5), 5231–5248. https://doi.org/10.1029/JC092iC05p05231

Thorpe, S. A. (2002). The axial coherence of Kelvin–Helmholtz billows. *Quarterly Journal of the Royal Meteorological Society*, *128*(583), 1529–1542. https://doi.org/10.1002/qj.200212858307

Thorpe, S. A. (2005). *The turbulent ocean*. Cambridge, U. K: Cambridge University Press.

Thurairajah, B., Bailey, S. M., Siskind, D. E., Randall, C. E., Taylor, M. J., & Russell, J. M. III (2013). Case study of an ice void structure in polar mesospheric clouds. *Journal of Atmospheric and Solar - Terrestrial Physics*, *104*, 224–233. https://doi.org/10.1016/j.jastp.2013.02.001

Triplett, C. C., Li, J., Collins, R. L., Lehmacher, G. A., Barjatya, A., Fritts, D. C., et al. (2018). Observations of reduced turbulence and wave activity in the Arctic middle atmosphere following the January 2015 sudden stratospheric warming. *Journal of Geophysical Research: Atmospheres*, *123*, 13,259–13,276. https://doi.org/10.1029/2018JD028788

Whiteway, J. A., Pavelin, E. G., Busen, R., Hacher, J., & Vosper, S. (2003). Airborne measurements of gravity wave breaking at the tropopause. *Geophysical Research Lettera*, *30*(20), 2070. https://doi.org/10.1029/2003GL018207

Williams, B. P., Fritts, D. C., She, C.-Y., & Goldberg, R. A. (2006). Gravity wave propagation through a large semidiurnal tide and instabilities in the mesosphere and lower thermosphere during the winter 2003 MaCWAVE rocket campaign. *Annales Geophysicae*, *24*(4), 1199–1208. https://doi.org/10.5194/angeo-24-1199-2006

Witt, G. (1962). Height, structure and displacements of noctilucent clouds. *Tellus*, *14*, 1–18. https://doi.org/10.3402/tellusa.v14i1.9524

Woods, J. D. (1968). Wave-induced shear instability in the summer thermocline. *Journal of Fluid Mechanics*, *32*(4), 791–800. https://doi.org/10.1017/S0022112068001035

Woods, J. D., & Wiley, R. L. (1972). Billow turbulence and ocean microstructure. *Deep Sea Research and Oceanographic Abstracts*, *19*, 87–121. https://doi.org/10.1016/0011-7471(72)90043-5

Yamada, Y., Fukunishi, H., Nakamura, T., & Tsuda, T. (2001). Breakdown of small-scale quasi-stationary gravity wave and transition to turbulence observed in OH airglow. *Geophysics Research Letters*, *28*(11), 2153–2156. https://doi.org/10.1029/2000GL011945

Yue, J., Thurairajah, B., Hoffmann, L., Alexander, J., Chandran, A., Taylor, M. J., et al. (2014). Concentric gravity waves in polar mesospheric clouds from the Cloud Imaging and Particle Size experiment. *Journal of Geophysical Research: Atmospheres*, *119*, 5115–5127. https://doi.org/10.1002/2013JD021385